Article

Daily Sea Ice Concentration Product over Polar Regions Based on Brightness Temperature Data from the HY-2B SMR Sensor

Suhui Wu [1,2,3], **Lijian Shi** [2,3,*], **Bin Zou** [2,3], **Tao Zeng** [2,3], **Zhaoqing Dong** [4] **and Dunwang Lu** [1,2,3]

1   National Marine Environmental Forecasting Center, Beijing 100081, China
2   National Satellite Ocean Application Service, Beijing 100081, China
3   Key Laboratory of Space Ocean Remote Sensing and Application, Ministry of Natural Resources, Beijing 100081, China
4   College of Oceanography, Hohai University, Nanjing 210098, China
*   Correspondence: shilj@mail.nsoas.org.cn; Tel.: +86-010-8248-1859

Abstract: Polar sea ice profoundly affects atmospheric and oceanic circulation and plays a significant role in climate change. Sea ice concentration (SIC) is a key geophysical parameter used to quantify these changes. In this study, we determined SIC products for the Arctic and Antarctic from 2019 to 2021 using data from the Chinese marine satellite Haiyang 2B (HY-2B) with an improved bootstrap algorithm. Then the results were compared with similar operational SIC products and ship-based data. Our findings demonstrate the effectiveness of the improved algorithm for accurately determining SIC in polar regions. Additionally, the results of the study demonstrate that the SIC product obtained through the improved bootstrap algorithm has a high correlation with other similar SIC products. The daily average SIC of the different products showed similar inter-annual trends for both the Arctic and Antarctic regions. Comparison of the different SIC products showed that the Arctic BT-SMR SIC was slightly lower than the BT-SSMIS and BT-AMSR2 SIC products, while the difference between Antarctic SIC products was more pronounced. The lowest MAE was between the BT-SSMIS SIC and BT-SMR SIC in both regions, while the largest MAE was between the NT-SMR and BT-SMR in the Arctic, and between the NT-SSMIS and BT-SMR in the Antarctic. The SIE and SIA time series showed consistent trends, with a greater difference in SIA than SIC and a slight difference in SIA between the BT-AMSR2 and BT-SMR in the Arctic. Evaluation of the different SIC products using ship-based observation data showed a high correlation between the BT-SMR SIC and the ship-based SIC of approximately 0.85 in the Arctic and 0.88 in the Antarctic. The time series of dynamic tie-points better reflected the seasonal variation in sea ice radiation characteristics. This study lays the foundation for the release of long-term SIC product series from the Chinese autonomous HY-2B satellite, which will ensure the continuity of polar sea ice records over the past 40 years despite potential interruptions.

Keywords: sea ice concentration; HY-2B; bootstrap; Arctic; Antarctic

1. Introduction

The Arctic region is warming at more than twice the global average rate due to the physical mechanism of the ocean–sea ice–atmosphere interaction, and the warming amplification trend is most noticeable in winter [1,2]. Regional warming in the Antarctic is substantial, with sea ice melting accelerating in the Antarctic Peninsula and its southwest region [3]. As an essential component of the global climate system, sea ice not only influences atmospheric and oceanic circulation, but is also an important indicator of climate change [4]. Sea ice uses the albedo effect to regulate the overall radiation balance of the Earth and the exchange of heat, momentum, and gases between the atmosphere and oceans in polar regions [5]. Since 1972, satellite observations have demonstrated a marked decreasing tendency in Arctic sea ice extent (SIE), sea ice area (SIA), and multi-year ice thickness [6,7]. However, Antarctic sea ice exhibits an overall weak rising tendency with

substantial seasonal and regional variations due to a combination of external forcing (e.g., ozone) and internal variability (e.g., multi-year intergenerational oscillations in the North Atlantic) [8]. The duration of Arctic sea ice melting is expanding at a rate of 5–10 days per decade, making Arctic commercial shipping a promising prospect. The opening of the Northeast Passage in summer will shorten the voyage and reduce greenhouse gas emissions [9]. Therefore, studying polar sea ice change patterns is important for the practical understanding and exploration of sea ice in the universal climate system, the evolution of ecosystems, and economic development.

Sea ice concentration (SIC), one of the most important parameters for describing sea ice, is defined as the proportion of sea ice cover per unit area. SIE and SIA can be estimated from SIC. Due to the harsh environment of polar regions, in addition to limited in situ observations, multiple satellites are relied upon to obtain multifactor distribution characteristics and changes in the polar regions on an all-weather, near real-time, and long-term continuous basis [10]. Microwave radiometry is the largest data source of all satellite data applied to polar region observations [11]. The Electrically Scanning Microwave Radiometer (EMSR), which was launched in 1972, was the first sensor to acquire global sea ice distribution with a relatively high temporal resolution. However, the sensor was merely a single-channel horizontally polarized radiometer, and the accuracy of the sea ice information acquired was restricted [12,13]. Since 1978, the Scanning Multichannel Microwave Radiometer (SMMR), the Special Sensor Microwave/Imager (SSMI), the Special Sensor Microwave/Imager Sounder (SSMIS), the Advanced Microwave Scanning Radiometer for EOS (AMSR-E), and the subsequent Advanced Microwave Scanning Radiometer 2 (AMSR2) have been successfully used to retrieve long-term time series SIC products. At present, the Scanning Microwave Radiometer (SMR) mounted on Chinese HY-2B satellites and the Microwave Radiation Imager (MWRI) mounted on FY-3 satellites have been successfully used to measure SIC [14–17]. The parameters of these different satellite sensors applied to sea ice monitoring are summarized in Table 1. In this table, only the SMMR sensor was sampled every other day before July 1987, with daily temporal resolution available since October 1978. The international SSMIS-F18 and AMSR2 sensors that are currently in orbit have exceeded their service lives, and there are no plans for subsequent launches. The microwave radiometer data from sea ice records, which have lasted for more than 40 years, are at risk of being discontinued [18]. The microwave radiometers carried by the Chinese HY-2B and FY-3 series satellites have similar observation channels to those of international microwave radiometers, and they may become one of the data sources for polar sea ice observation.

Table 1. An overview of satellite microwave sensors for monitoring sea ice.

Sensor	Platform	Frequencies in GHz	View Angle	Operation Date
ESMR	Nimbus-5	19.4	0–50°	1972–1976
SMMR	Nimbus-7	6.6, 10.7, 18.0, 21.0, 37.0	50.2°	1978–1987
SSM/I	DMSPF8-F11 13–F15	19.4, 22.2, 37.0, 85.5	53.1°	1987–2009
SSMIS	DMSP F16–F19	19.4, 22.2, 37.0, 91.7	53.1°	2003–today
AMSR-E	Aqua	6.9, 10.7, 18.7, 23.8, 36.5, 89.0	55°	2002–2011
AMSR2	GCOW-W1	6.9, 7.3, 10.7, 18.7, 23.8, 36.5, 89.0	55°	2012–today
SMR	HY-2B	6.4, 10.7, 18.7, 23.8, 37.0	53°	2018–today
MWRI	FY-3B/C/D	10.7, 18.7, 23.8, 36.5, 89.0	52°	2010–today

Over the last few decades, a considerable number of different algorithms have been developed to calculate SIC from microwave satellite T_B data. A majority of algorithms estimate SIC by comparing T_B between open water and sea ice at typical viewing angles (50–55°) using horizontal (H) and vertical (V) polarizations. Typically, T_B polarization ratios (PRs) and temperature gradient ratios (GRs) are used. These algorithms primarily contain NASA Team (NT) [19], bootstrap (BT) [20–23], Bristol [24], and OSI-SAF [25,26], which mainly utilize T_B data from the 19 and 37 GHz low-frequency channels to obtain SIC

products with a spatial resolution of 25 km due to the moderately low raw spatial resolution. The spatial resolution of SIC products has improved significantly with the application of high frequency channels (85/89 GHz) in different algorithms, mainly including the Enhanced NASA Team (NT2) [27,28] and Arctic Radiation and Turbulence Interaction Study (ASI) [29,30] algorithms. Among the many algorithms, the NASA Team algorithm and the NT2 algorithm can measure the overall SIC and the first-year ice and multi-year ice concentrations.

Two different forms of internal comparison of sea ice concentration usually exist [31]. One is to compare SIC products based on different algorithms without using independent data sources [32,33]. This form of inter-comparison can provide information on time series and trends in the overall SIC distribution as well as SIA and SIE and consistency between products. Simultaneously, it can reveal regional differences and seasonal cycles in the SIC values calculated by different algorithms. Nevertheless, it does not provide information about the accuracy of the SIC products. The other type of algorithm inter-comparison study involves high-resolution satellite information, such as optical images, or active microwave sensors, such as synthetic aperture radar (SAR) [34–36]. Additionally, ice charts [37,38] and ship-based observations [29,39–42] are used for this type of comparison. To demonstrate their functionality under different ice and weather conditions, different algorithms were repeatedly compared with each other [33,43].

Beitsch et al. [40] evaluated the SIC products of six different algorithms using 21,600 ship-based observations in the Antarctic and showed that the bootstrap algorithm was in the most-consistent agreement with the shipboard observations. Spreen et al. [29] compared SIC data based on different algorithms with data based on shipboard observations. He found that the ASI, NT2, and BT algorithms had correlations of 0.80, 0.79, and 0.81, respectively, with the bootstrap algorithm showing the best overall performance. Kern et al. [31] assessed ten SIC products using shipboard observational datasets and showed that the BT-AMSR-E and BT-SSMI products have a small bias and relatively high correlation coefficients. Kern et al. [44] evaluated 10 types of passive microwave (PM) SIC products using SIC calculated from over 300 Landsat images and showed that the BT-based SIC products had the lowest bias. According to many quantitative evaluations, the BT algorithm is one of the most accurate at estimating SIC. However, it was challenging to apply the algorithm to China's autonomous HY-2B SMR when the tie-points were chosen as fixed coefficients at an early algorithm stage. Currently, the selection of dynamic tie-points of the bootstrap algorithm requires a detailed description, and the application to HY-2B needs further study.

In this paper, we propose an improved BT SIC algorithm using the SMR T_B data from HY-2B. The published SIC datasets, the ship-based observation data gathered for validation, and the SMR T_B data are all described in Section 2. Section 3 describes the whole process of the BT algorithm, which mainly includes the dynamic selection methods of tie-points, the use of weather filters, and the removal of land spillover effects. In Section 4, a long-term time series analysis of the BT algorithm tie-points is performed, the SIC values obtained in this study are compared in detail with other SIC products, and the accuracy of SIC products is assessed using ship-based observation data. In Section 5, a long-term time series analysis of the SIE and SIA is performed, with an assessment of the SIE of the different BT SIC products in the marginal ice zone (MIZ). The conclusions are summarized in Section 6.

2. Data

2.1. HY-2B SMR Sensor

HY-2B is the first operational marine dynamic environment monitoring satellite for China, and combines active and passive microwave remote sensors in an integrated system, with high-precision orbit measurement, orbit setting capability, and all-weather, all-day, global detection capability. The satellite carries radar altimetry, a microwave scatterometer, a scanning microwave radiometer (SMR), and a calibration microwave radiometer. The SMR has five operational frequencies, 6.6, 10.7, 18.7, 23.8, and 37 GHz, but does not include the 23.8 GHz frequency, as it is only vertically polarized, and the other four frequencies

have both horizontal (H) and vertical (V) polarizations. The SMR sensor has a swath width of over 1600 km. It has a sensitivity of better than 0.8 K in the 37 GHz band and better than 0.5 K in the rest of the frequency band, allowing for the retrieval of global data for sea surface temperature, sea surface wind field, sea surface water vapor content, liquid water, and rainfall intensity. The main specifications of the HY-2 SMR are listed in Table 2.

Table 2. Specifications of the HY-2B SMR instrument.

Configuration Parameter	Values				
Frequency (GHz)	6.925	10.7	18.7	23.8	37.0
Polarization	V H	VH	VH	V	VH
Bandwidth (MHz)	350	100	200	400	1000
Sensitivity (K)	0.5	0.6	0.5	0.5	0.8
Calibration Error (K)			1		
Ground Resolution (km)	90×150	70×110	36×60	30×52	20×35
Dynamic Range (K)			3–350		
Scan Mode			Conical scanning		
Orbit Width (km)			1600		
View angle (°)			53		

In this study, Arctic and Antarctic T_B data from 2019–2021 were collected. Related studies have shown that the bias of SIC obtained from swath data (Level 2A) and using daily average data (Level 3A) is less than 1% [29]. Therefore, within the margin of error, in this paper, we utilize Level 3A daily average T_B data for the retrieval of SIC, excluding factors such as data loss due to the sensor's inherent instability, and we use 1059 days (Arctic) and 1058 days (Antarctic) of data, accounting for 96.8% (Arctic) and 96.7% (Antarctic) of the total number of days over the three years, respectively.

2.2. Published SIC datasets

In this study, SIC datasets were analyzed based on three sensors, SSMIS, AMSR2, and HY-2B SMR; four SIC retrieval algorithms were included, and all datasets cover the Arctic and Antarctic and a time range from 2019 to 2021. Table 3 lists the main datasets used in our study.

Table 3. Summary of the SIC datasets applied in this study.

Datasets	Source	Period	Sensor	Algorithm	Resolution (km)
BT-SMR	This study	2019–2021	SMR	BT	25
NT-SMR	NSOAS	2019–2021	SMR	NT	25
NT-SSMIS	NSIDC	2019–2021	SSMIS	NT	25
BT-SSMIS	NSIDC	2019–2021	SSMIS	BT	25
NT2-AMSR2	NSIDC	2019–2021	AMSR2	NT2	25
BT-AMSR2	NSIDC	2019–2021	AMSR2	BT	25
ASI-AMSR2	Bremen	2019–2021	ASMR2	ASI	6.25

The NT-SMR dataset was obtained by Shi et al. [17] based on the HY-2B satellite-borne SMR T_B data with the NT algorithm. A cross-calibration study of HY-2B SMR T_B was conducted using DMSP-F17 SSMIS T_B data as a reference. The results were cross-validated against ship-based observation data, NT products released by the National Snow and Ice Data Center (NSIDC), and SAR products. Overall, the accuracy was satisfactory.

The NT-SSMIS dataset is the NSIDC-0051 product of the NSIDC [45]. The dataset is based on T_B data from SMMR, SSM/I, and SSMIS sensors since 1978. SIC values at the North and South Poles are generated by the NT algorithms.

The BT-SSMIS dataset is the NSIDC-0079 product of the NSIDC [46], which generates North and South Pole SIC values based on the BT algorithm with daily dynamic tie-points.

The NT2-AMSR2 and BT-AMSR2 datasets are from the AMSR-E/AMSR2 Unified L3 Daily 25 km Brightness Temperatures & Sea Ice Concentration Polar Grids version 1, which are available and accessible on the NSIDC website. The BT-AMSR2 dataset is not directly provided in a manner different from NT2-AMSR2. It uses AMSR2 Level-1R input T_B calibrated by JAXA in AMSR-E and AMSR2 Level-1R products. Both datasets have a spatial resolution of 25 km with polar stereo grid projection.

The ASI-AMSR2 dataset was obtained by the Institute of Environmental Physics at the University of Bremen (https://seaice.uni-bremen.de, accessed on 6 December 2022) based on the ASI algorithm with 89 GHz T_B data inversion with a spatial resolution of 6.25 km. The high-frequency channels are used with increased sensitivity to weather variability. The ASI algorithm uses the same weather filter as the NT algorithm.

2.3. Ship-Based Sea Ice Cover Observations

This study collected shipboard data from underway observations in the Antarctic and Arctic regions from 2019 to 2021. Figure 1 shows the spatial distribution of ship-based observation data, with approximately 3983 independent observations, including 3367 in the Arctic and 616 in the Antarctic. The North and South Poles have 464 and 91 pairs of data available after averaging the data each day, respectively. In the Arctic, observations are mainly located in the Barents Sea, Laptev Sea, East Siberian Sea, Chukchi Sea, Beaufort Sea, and Central Arctic. However, there are fewer or almost no observations in other regions. In the Antarctic, observations are mainly located in the South Atlantic, Weddell Sea, and the Antarctic Peninsula Annex. The PM SIC datasets used in this paper have spatial resolutions of 6.25 and 25 km. However, shipboard data have higher temporal and spatial resolutions, making direct comparisons difficult [47]. According to the methodology of Beitsch et al. [40], we spatiotemporally matched PM SIC to selected ship-based observations by calculating the minimum distance between the geographical location of the ship-based observations and the grid cells of the PM SIC products, and finally averaged all ship-based and PM SIC on a daily basis. The ship-based and PM SIC values are compared with each other using scatter plots, linear regression analysis, heatmap analysis, and statistical analysis for summer data, winter data, and overall data in Section 4.3.
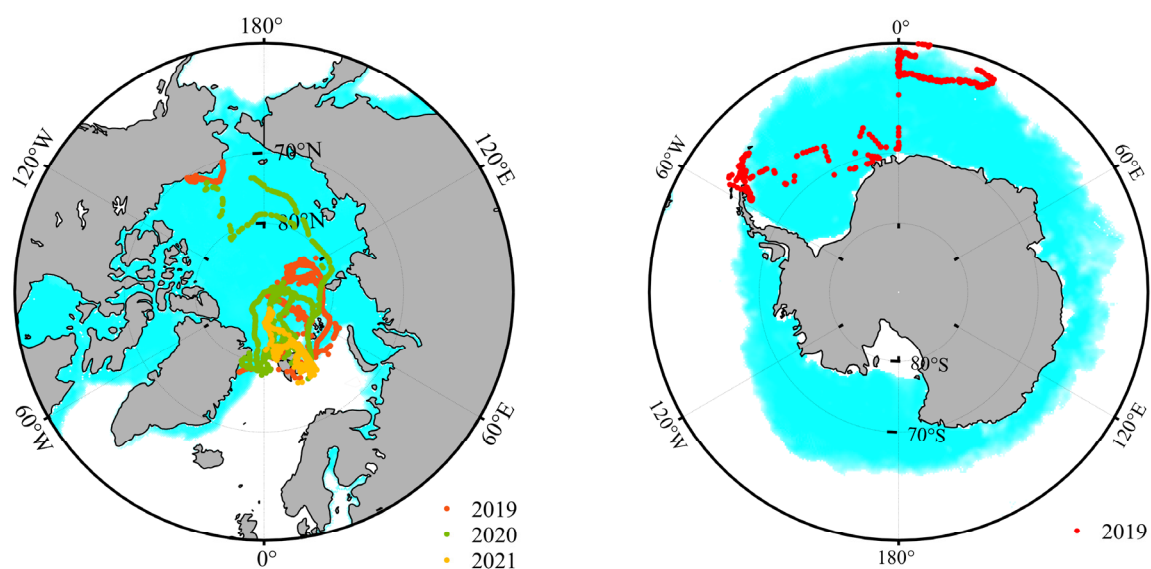

Figure 1. Spatial distribution of ship-based observation data, with red denoting 2019, green denoting 2020, and yellow denoting 2021. The background image is the SIE map on 5 February 2019 ((**left**), Arctic; (**right**), Antarctic).

3. Methods

3.1. Basic BT Algorithm Technique

Assuming that within each data grid, the proportion of open water is C_O and the proportion of sea ice is C_I, the observed T_B can be expressed as follows:

$$T_B = T_B^O C_O + T_B^I C_I \tag{1}$$

In Equation (1), T_B^O and T_B^I denote the T_B of open water and sea ice, respectively. Since $C_O + C_I = 1$,

$$C_I = \frac{T_B - T_B^O}{T_B^I - T_B^O} \tag{2}$$

In Equation (2), I and O represent the two different surface types of sea ice and seawater, respectively. From Equation (2), if the tie-points T_B^I and T_B^O are known, the SIC of each grid cell within the footprint can be calculated from the observed T_B. The tie-points are not fixed due to the radiative properties of sea ice and surface snow, the spatial variability in the physical temperature, and the spatial and temporal variabilities in atmospheric conditions. The nonlinearity and large variability in T_B are mainly caused by the emission of radiation scattered in the interior of the ice [21]. The 37 and 19 GHz channels are used in the BT algorithm to identify the tie-points of T_B^O and T_B^I.

The schematic diagram of the BT algorithm is represented in Figure 2. The data points distributed along the AD line in the figure represent close to 100% SIC, but they have different emissivity or temperature values. In Equation (2), point I is 100% SIC of a specific type of sea ice based on its emissivity or temperature. The line OI represents linearly varying SIC values of this sea ice type. The algorithm is effective when most of the 100% SIC is distributed along the AD. Therefore, the accuracy and objective acquisition of the AD line determines the accuracy of SIC retrieval. The T_B represented by data point I is the value of the intersection of lines AD and BO. The selection of the dynamic tie-points is specifically described in Section 3.2. The scattered points along the OW line in the diagram represent data in open seawater. The T_B of these points can increase due to severe weather conditions, such as storms. They can affect the estimation of the actual SIC values. A detailed description of the method for removing the effect of weather conditions can be found in Section 3.3. To simplify the calculation of the actual SIC values, $T_B - T_B^O$ denotes the distance between points O and B, and $T_B^I - T_B^O$ denotes the distance between points O and I [21].
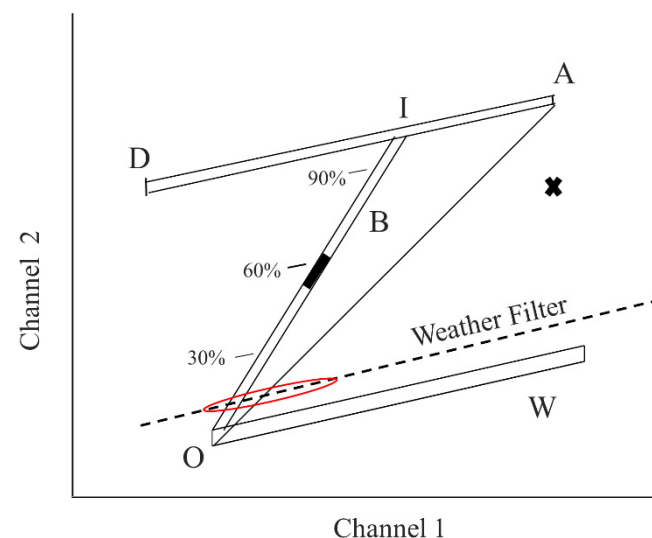

Figure 2. Schematic diagram of the bootstrap algorithm.

The BT algorithm in the specific application process mainly involves the polarization mode (HV37) and frequency mode (V1937), and Figure 3 represents the scatter of the HV37 pattern and V1937 pattern in the Arctic region observed by HY2B SMR on 1 January 2020 (land mask has been performed). The high correlation between the 37 GHz (H) and 37 GHz (V) channels, named the polarization mode of the BT algorithm (HV37), is most often used in retrieving Arctic SIC. This combination of channels is ideally suited for the retrieval of high SIC values because the standard deviation of linear clustering of data points distributed along the AD line is less than 2.5 K, which is appropriate for Arctic winter SIC of more than 95% [21]. The slope of the AD line is almost always close to 1.0 for sea ice close to 100% SIC. This scenario has the same effect on the SMMR, SSMI, SSMIS, and SMR sensors. Due to the considerable regional variation in horizontal polarization T_B over the low SIC area, 19 V and 37 V GHz are usually used for inversion. Statistical analyses have shown that the V1937 pattern provides more coherent SIC values than the HV37 pattern in low-concentration ice areas [22,48]. In the Antarctic and Arctic seasonal ice regions, where the ice cover consists mainly of first-year ice, the radiance is more uniform than in the central Arctic region. Points in these regions are less affected by volume scattering from the ice interior. Usually, they do not form nonlinear clusters for multi-year ice observations, so the V1937 pattern is used to obtain low SIC values. Comiso et al. [23] demonstrated that the SMMR and SSMIS sensors' inverse SIC values for the data points along the AD line in the V1937 pattern were smaller than those in the HV37 pattern. The results of the SMR sensor were the same as those of the microwave radiometers, mainly because the different polarization modes are sensitive to ice layers and roughness [49].
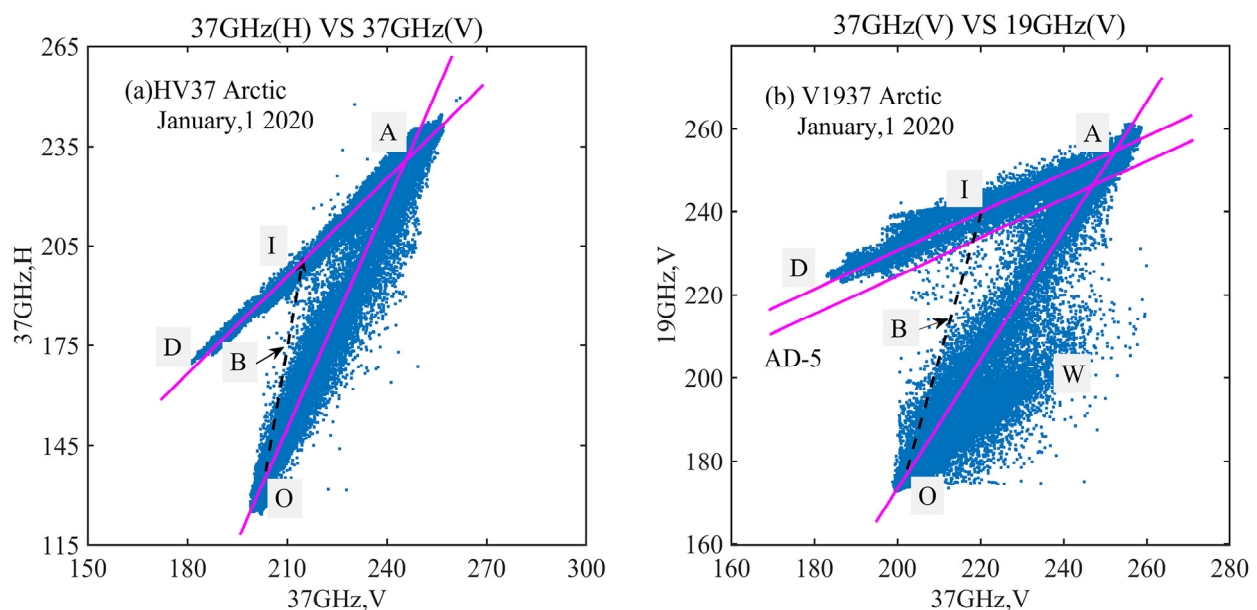

Figure 3. Scatter diagrams of polarization mode and frequency mode on 1 January 2020. (**a**) Polarization mode. (**b**) Frequency mode. AD line for sea ice close to 100% SIC, the letter I indicates different types of ice, the letter B indicates the SIC value at any point, the letter O indicates water tie-point.

When performing SIC calculations, ideally, the scatter plots are concentrated in the OAD triangle. However, in the actual SMMR, SSM/I, SSMIS, and SMR data, some points are subject to random noise and large physical temperature and spatial variability, so they require special consideration. These points in Figure 1 fall to the right of OA, mainly consisting of young ice and floating ice in MIZ [21]. According to the Comiso et al. [21] processing method, the SIC values of these data points are calculated by replacing OI with OA. It is possible to provide more reliable SIC values by processing the data points in this way.

In the central Arctic region, i.e., away from the ice edge, the HV37 pattern is used, and the points above AD-5 in the middle line of Figure 3b are delineated during the process of SIC inversion. In the MIZ, i.e., points below AD-5, the SIC results are calculated using the V1937 pattern. This −5 K offset is mostly due to the presence of 5–10% open water in the central Arctic winter region [21]. The parameters of −5 K used in this study are consistent with the BT-based SIC datasets published by Comiso et al. [21] and NSIDC [48].

3.2. Choice of Tie-Points

The selection of tie-points is a critical process for the inversion of SIC, which is related to the accuracy of the final SIC values. In the BT algorithm, T_I and T_O are mainly determined from the scatter plot. As described in the previous section, sea ice with 100% SIC is distributed along line AD. Then, point I can be obtained by determining the feature values of line AD and point O. Determination of lines AD and AO involves selecting points along line AD and near AO. Then, a linear regression is performed to determine the linear equation of AD and AO and solve for the coordinates of intersection point A.

In the Arctic, for the HV37 pattern, given initial point A_0 (250, 235) and point D_0 (186, 173) (as close as possible to the center of linear clustering of AD, as shown by the black dashed line in Figure 4a), initial point A_0 (250, 235) and point O_0 (202, 130) (as close as possible to the center of linear clustering of AO), determined by the initial point of lines A_0D_0 and A_0O_0, which are increased by ±10 intercepts (magenta dashed line in Figure 4a), the scatter points distributed along AD (light blue point in Figure 4a) and AO (green point in Figure 4a) are selected, and the linear AD and AO equations used for SIC inversion are obtained by linear regression. For the V1937 pattern, similar to the above method, given initial point A_0 (250, 252) and point D_0 (183, 222), and initial point A_0 (250, 252) and point O_0 (203, 177), the A_0D_0 and A_0O_0 determined from the initial point increase the ±10 intercepts (magenta dashed line in Figure 4b). To obtain the linear equation, we linearly regressed scatter points along the AD (light blue point in Figure 4b) and AO (green point in Figure 4b). In the Antarctic, the frequency pattern is given by the initial A_0 (255, 256), D_0 (206, 235), and O_0 (205, 178). The ±10 K parameter is chosen based on the HY-2B SMR T_B scatter distribution. In the melting period, the T_B of sea ice increases, and the clustering features are relatively scattered compared with winter, and ±10 K considers this scatter.
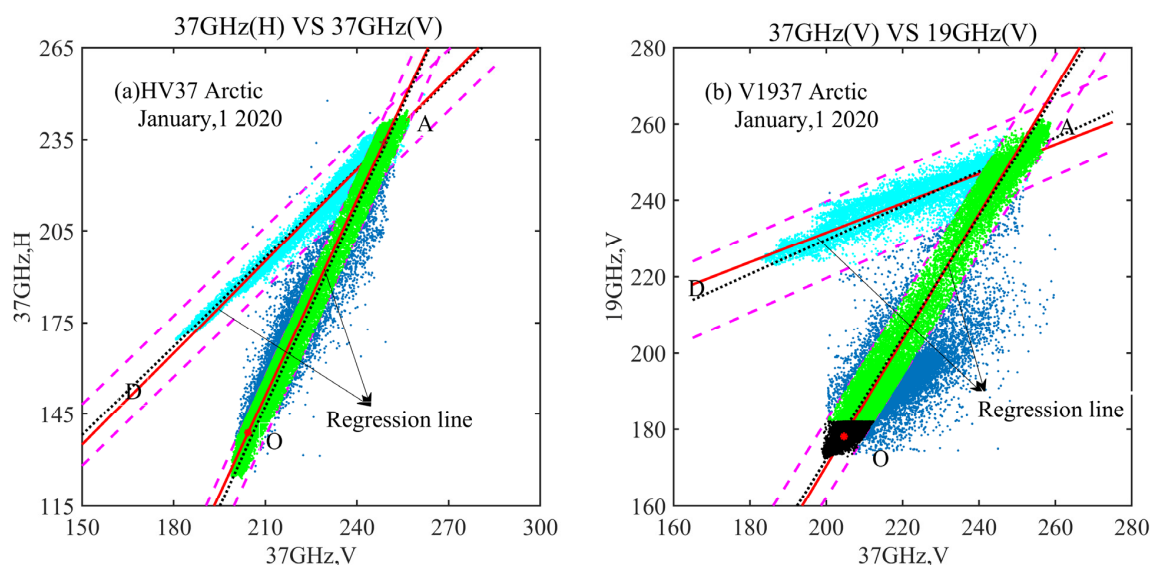

Figure 4. Selection of tie-points for the BT algorithm. (**a**) Polarization mode. (**b**) Frequency mode. The black dashed lines AD and AO represent the lines formed by the initial points. Magenta dashed line indicates the result of AD or AO ± 10 K. The red line indicates the result of the linear regression of AD or AO.

The surface characteristics of the open water inside the high-SIC area are smoother because the ice floes have significantly weakened many wave effects. Therefore, the T_B of this part of the open water is closer to T_O. The value of the actual T_O is chosen at approximately the intersection of OW and OA. In the V1937 pattern, the points with T_B (19 GHz) < 182 K (corresponding to the points in the black area in Figure 3b) are selected, and the average value of 37 GHz (V) is calculated as the tie-point of T_O at 37 GHz, which is used in the linear AO equations of the V1937 pattern and the HV37 pattern to obtain T_O at 19 GHz (V) and 37 GHz (H), respectively. This method realizes the dynamic selection of T_I and T_O according to the daily T_B scattering point distribution. Since the daily T_B variation is influenced by short-term weather, this study averaged all dynamic tie-points on a $[-7, +7]$ day sliding mean, and the practice of averaging dynamic tie-points on a $[-7, +7]$ day sliding mean is consistent with that of Lavergne et al. [25] and Zhao et al. [16].

3.3. Weather Filters

In the marginal regions of the open ocean and sea ice, weather effects, such as liquid water in clouds, sea surface water vapor, rainfall, and wind, cause a significant increase in T_B. This algorithm applies to regions with unrealistic SIC values by using weather filters and atmospheric corrections. For the BT algorithm, the data points from open water are mainly clustered along the OW, as shown in Figure 2. It is possible to separate open water from the ice-covered area by straight lines, but the slope and intercept of the straight lines are more challenging to determine. Subtle changes in the slope and intercept have the most significant impact on the points in the red curve in Figure 2 because the SIC value is set to 0% for all points below the straight lines. During the summer, when sea ice melts, the straight line determined by the slope and intercept fails to completely remove the spurious sea ice.

In this study, the removal of spurious SIC is achieved using the spectral gradient ratio (GR) commonly used in the NT and ASI algorithms, which consists of two primary filters, $GR(37V, 19V)$ and $GR(22V, 19V)$:

$$GR(37V, 19V) = \frac{TB(37V) - TB(19V)}{TB(37V) + TB(19V)} \tag{3}$$

$$GR(22V, 19V) = \frac{TB(22V) - TB(19V)}{TB(22V) + TB(19V)} \tag{4}$$

The thresholds applicable to the HY2B SMR weather filter are described as follows:

(1)   The SIC is set to 0% if $GR(37V, 19V) > 0.05$ (Arctic) or $GR(37V, 19V) > 0.055$ (Antarctic), which mainly removes the effects of liquid water and ice crystals in the clouds.

(2)   The SIC is set to 0% if $GR(22V, 19V) > 0.035$ (Arctic) or $(GR(27V, 19V) > 0.035)$ (Antarctic), which mainly removes the effect of water vapor over open water.

Based on the two weather filters, the monthly maximum SIE data were also used for masking, and spurious sea ice in open water was primarily removed.

3.4. Land Spillover Correction

Land contamination is a blurring effect arising from the relatively coarse width of the sensor antenna pattern, resulting in overestimation of SIC in the nearshore region, especially in summer. In this study, the method of Cavalieri et al. [50] was used, assuming that the minimum SIC observed near shorelines without sea ice residuals results from land spillover, which is subtracted from the image.

4. Results

4.1. BT Algorithm Tie-Points Time Series Analysis

The 37 GHz(V) open water (T_o) is plotted for 2019–2021 using the method of identifying dynamic tie-points introduced in Section 3.2. As shown in Figure 5, the yellow dash represents the tie-point of open water obtained from the actual scatter plot, and the red

curve is the result of performing a ±7 day sliding average. T_o has seasonal variation characteristics, especially in the Arctic. In general, the tie-point of open water was relatively low and varied slightly in winter. The T_o values increased and varied significantly in summer, which is consistent with the trend of Comiso et al. [21], who used fixed open water tie-point values in winter and summer [21]. The tie points of open water in the Arctic winter (November–April) and summer (May–October) are 204.79 ± 0.45 K and 205.87 ± 0.79 K, respectively. In the Antarctic winter (May–October) and summer (November–April), the tie-points of open water are 205.98 ± 0.43 K and 206.48 ± 0.45 K, respectively. The tie-points of open water in the Antarctic are ~1 K higher than those in the Arctic.
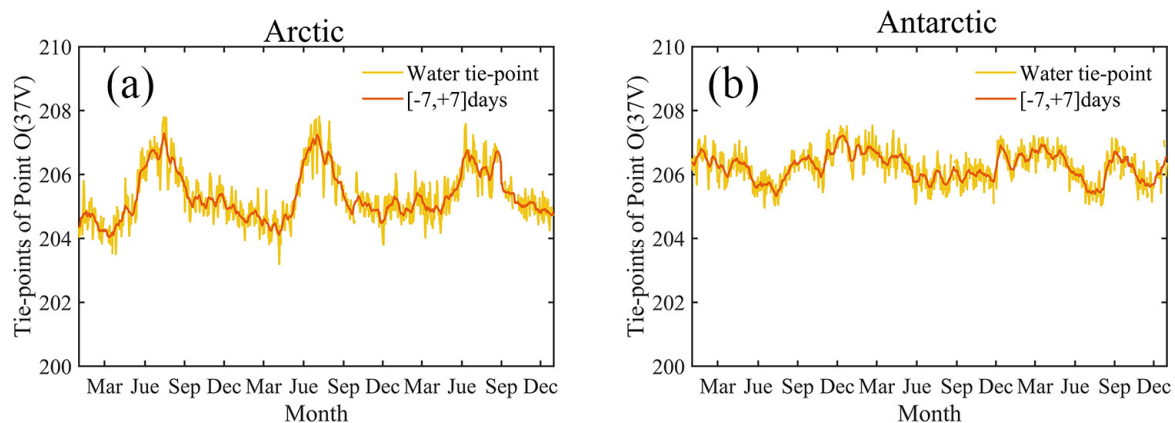

Figure 5. Daily HY-2B SMR bootstrap algorithm tie-points T_O for open water (orange line) and [−7, +7] day interval results (red line) during 2019–2021. The (**a**) diagram indicates the Arctic and the (**b**) diagram indicates the Antarctic.

As introduced in Section 3.1, the Arctic SIC is mainly calculated by the HV37 and V1937 patterns, and in this subsection, a time series analysis is conducted on the regression parameters with scatter points selected in different patterns, as shown in Figure 6a–l. For the HV37 pattern, the mean slope of line AD in winter was approximately 0.96 (close to 1) with small overall fluctuations (standard deviation of 0.02), which is consistent with the earlier values of fixed tie-points used by Comiso et al. [21]. In summer, the slope of line AD increases and fluctuates strongly, with interannual variability characterized by a maximum slope of approximately 1.4 (Figure 6b). The intercept of the line AD has an opposite trend to the slope (Figure 6c), which is relatively stable in winter and decreases sharply in summer as the slope increases, with a minimum value of approximately −100 K. The RMSE of the regressed linear AD is slightly smaller in winter than in summer, and the difference is mainly caused by the disappearance of the multi-year ice scatter feature around the linear AD in summer. Concerning the frequency pattern, the average slope of the linear AD is 0.42 ± 0.04 in winter and 0.46 ± 0.14 in summer (Figure 6h), and the intercept decreases with increasing slope. The RMSEs of the fitted linear AD (Figure 6g) were 3.24 ± 0.29 and 3.90 ± 0.84 in winter and summer, respectively, which were greater than the fitted parameters in the HV37 pattern. The trend of the linear AO is consistent in both the HV37 pattern and the V1937 pattern. The Antarctic SIC values are calculated from the V1937 pattern only, and the time series of the regression parameters are shown in Figure 6m–r. The average slope of the fitted line AD was 0.47 ± 0.07, with a slight overall difference; the seasonal trend of the line AO in winter was noticeable, with an average slope of 1.64 ± 0.02, and the slope decreased in summer. The RMSE of the regression line AD was greater than that of the line AO.
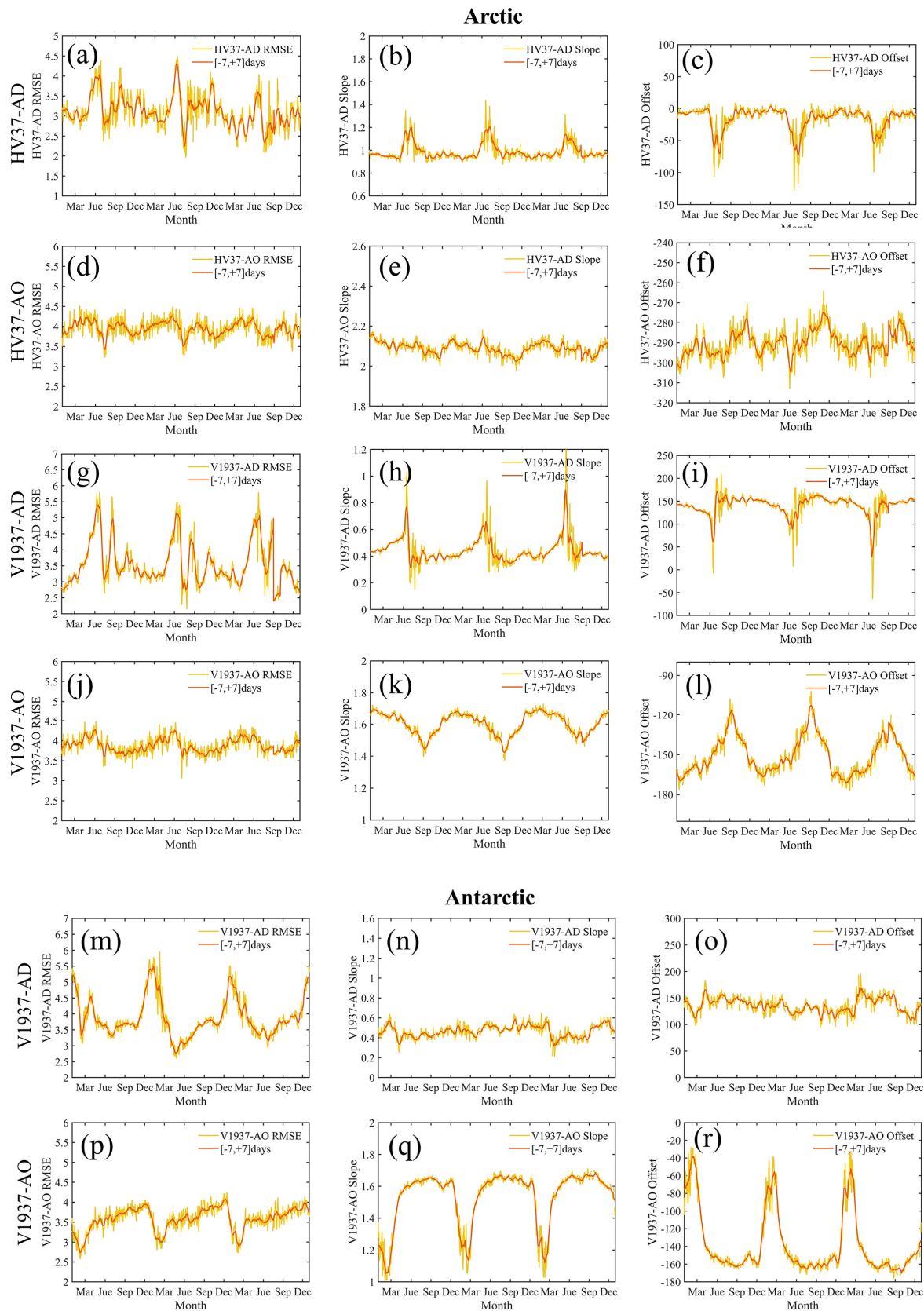
Figure 6. The linear regression parameters for SIC retrieval. The (**a**–**l**) diagrams indicate the Arctic, and the (**m**–**r**) diagrams indicate the Antarctic. The first column represents the RMSE of the respective linear regression equation; the second column represents the slope; and the third column represents the intercept.

4.2. Comparisons of the BT-SMR SIC Products

SIC datasets, derived from HY-2B SMR T_B with the BT algorithm, are compared with similar products in this subsection. Unlike the comparison based on monthly average SIC by Ivanova et al. [43], the comparison results in this section are based on daily average SIC, and both SIE and SIA can be derived from the daily average SIC. The SIE is calculated by summing over the grid cells with SIC > 15%. The SIA is calculated by summing the SIC over the ice-covered area in each grid cell. All data have been land-masked to exclude the influence of lakes and other inland waters on SIC estimates.

A time series analysis of six 25 km SIC products is conducted in Section 4.2.1 (Arctic) and Section 4.2.2 (Antarctic) using the bias and mean absolute error (MAE) and comparing the spatial distribution of SIC for specific months selected during the winter and summer. An interval assessment approach is used in Section 4.2.3 to quantitatively compare the different SIC products.

4.2.1. Arctic SIC and Spatial Distribution Differences

As shown in Figure 7a, the six 25 km SIC products have similar interannual variability trends. In November–April, SIC values are relatively stable, mainly in the range of 85–97%, and the NT2-AMSR2 values are relatively large at approximately 96%; NT-SMR and NT-SSMIS have the most negligible inversion results at 92%; the results obtained in this study are slightly lower than those of BT-SSMIS and BT-AMSR2 at approximately 94%. In May–October, SIC values are highly variable due to rising temperatures and increasing melting ponds. The variability is much higher for different SIC products, with SIC values mainly within the range of 65–90%. As in November–April, most SIC values for NT2-AMSR2 were more significant, approximately 90%, than those for NT-SMR or NT-SSMIS, which were approximately 70%. Compared to BT-SSMIS and BT-AMSR2, the BT-SMR results were lower than the BT-SSMIS and BT-AMSR2 results by approximately 80%, and the difference reached its maximum during August and September each year. The correlation coefficients of NT-SMR, NT-SSMIS, BT-SSMIS, BT-AMSR2, and NT2-AMSR2 with BT-SMR SIC were 0.94, 0.94, 0.97, 0.96, and 0.97, respectively. Overall, the SIC products based on the same algorithm had the most negligible bias and more consistent interannual trends.

Based on daily average SIC products in the Arctic, bias (Figure 7b) and MAE (Figure 7c) were calculated, and time series were plotted. Bias was calculated by subtracting BT-SMR from the five SIC products. From the bias parameters, the five products can be classified into two categories: the first category is BT-SSMIS, BT-AMSR2, and NT2-AMSR2, which all exhibit positive deviations from BT-SMR, with overall biases of 2.89, 3.25, and 3.26, respectively; the second category is NT-SMR and NT-SSMIS, which both exhibit negative deviations from BT-SMR, with overall biases of −8.87 and −7.96, respectively. In summary, a slight difference was found between BT-SSMIS and BT-SMR, and the most significant negative difference was between NT-SMR and BT-SMR. Moreover, the differences in SIC products based on the NT algorithm start increasing earlier in May–October and end later than those based on the BT and NT2 algorithms, which means that the results based on the NT algorithm are biased longer in May–October compared to the other products. NT-SSMIS, NT-SSMIS, BT-SSMIS, BT-AMSR2, and NT2-AMSR2 showed overall MAEs of 9.00, 8.20, 3.64, 4.71, and 4.16, respectively, compared to BT-SMR. Therefore, the MAE difference between the BT-SSMIS and BT-SMR products in the Arctic is the smallest, while the MAE difference between the NT-SMR products is the largest.
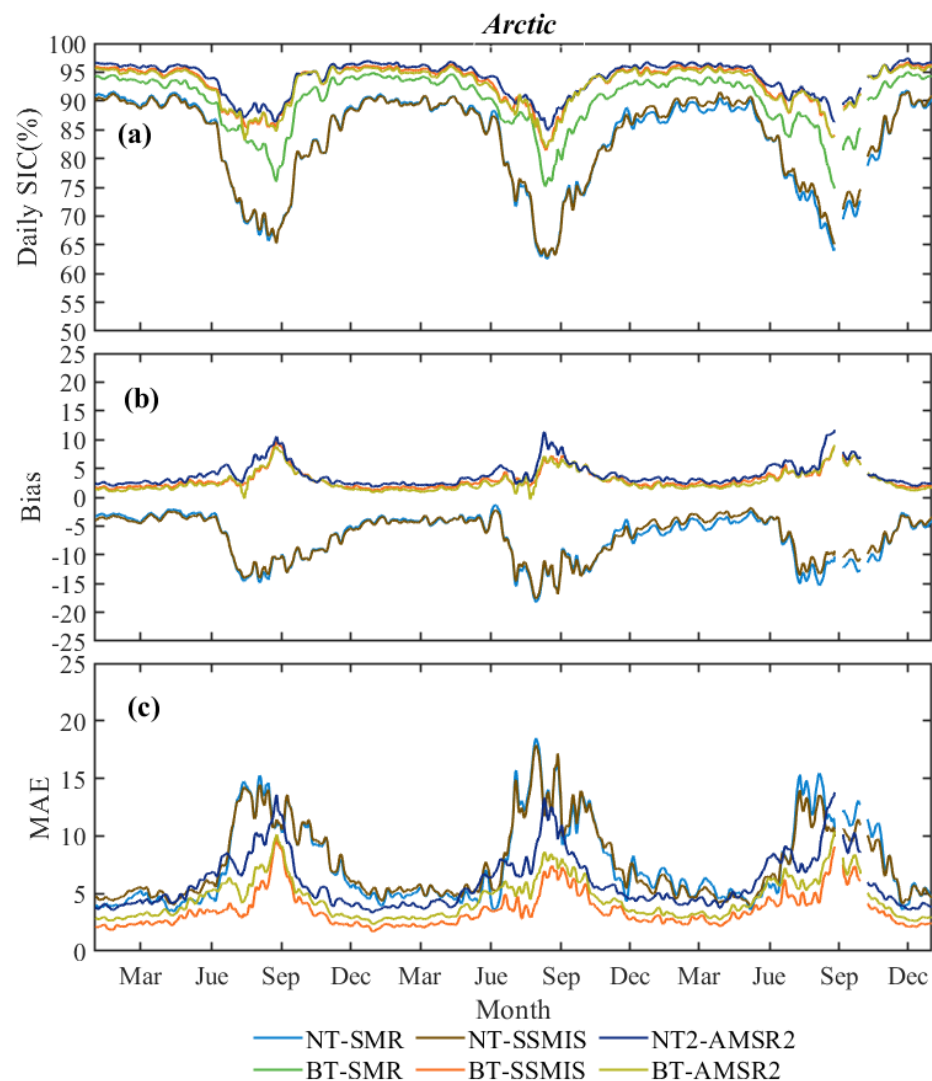
Figure 7. Arctic daily average SIC (**a**), bias (**b**) and MAE (**c**) from January 2019 to December 2021 for 25 km spatial resolution SIC datasets. Bias refers to the above SIC datasets minus BT−SMR daily average difference. MAE refers to mean absolute error.

In the Arctic, multi-year ice is dominant in winter with relatively small deviations, and the most significant deviations occur in August and September during the summer, based on time series analysis of SIC datasets. Figure 8 shows the typical winter and summer months of March and September. The map shows differences in the spatial distribution of SIC products. Figure 8a–e depicts the overall SIC differences, and Figures 8f–j and 8k–o represent the differences in March and September, respectively. The evaluation parameters are presented in Table 4. Overall, the differences among the five SIC products show a trend of gradually increasing from high to low latitudes, with BT-SMR, BT-AMSR2, and NT2-AMSR2 showing positive deviations and NT-SMR and NT-SSMIS showing negative deviations. For the BT-SMR, BT-AMSR2, and NT2-AMSR2 products, the deviation in the central Arctic region is almost zero, and the MIZ exhibits a positive deviation. For the NT-SMR and NT-SSMIS products, the central Arctic region shows a slight positive deviation, while the MIZ shows the most negative deviation; the most negative deviation occurs in the Sea of Okhotsk. When sea ice melt is in its final stages in September, BT-SMR, BT-AMSR2, and NT2-AMSR2 show a positive bias in the central Arctic, while a slightly negative bias is observed along the coast in Hudson Bay, Canadian Islands, Beaufort Sea, and Chukchi Sea. All regions experienced negative deviations for NT-SMR and NT-SSMIS, which were much higher than the March average or overall deviations. According to

the evaluated parameters in Table 4, the September bias for BT-SMR, BT-AMSR2, and NT2-AMSR2 was smaller than that overall and the March average, mainly due to the offset between positive and negative biases. According to the MAE and RMSE metrics, the slightest difference in overall assessments, March assessments, and September assessments was between BT-SSMIS and BT-SMR, the most remarkable negative difference was between NT-SMR and BT-SMR, and the most positive difference was between NT2-AMSR2 and BT-SMR. Generally, the March average outperformed both the September average and the overall average.
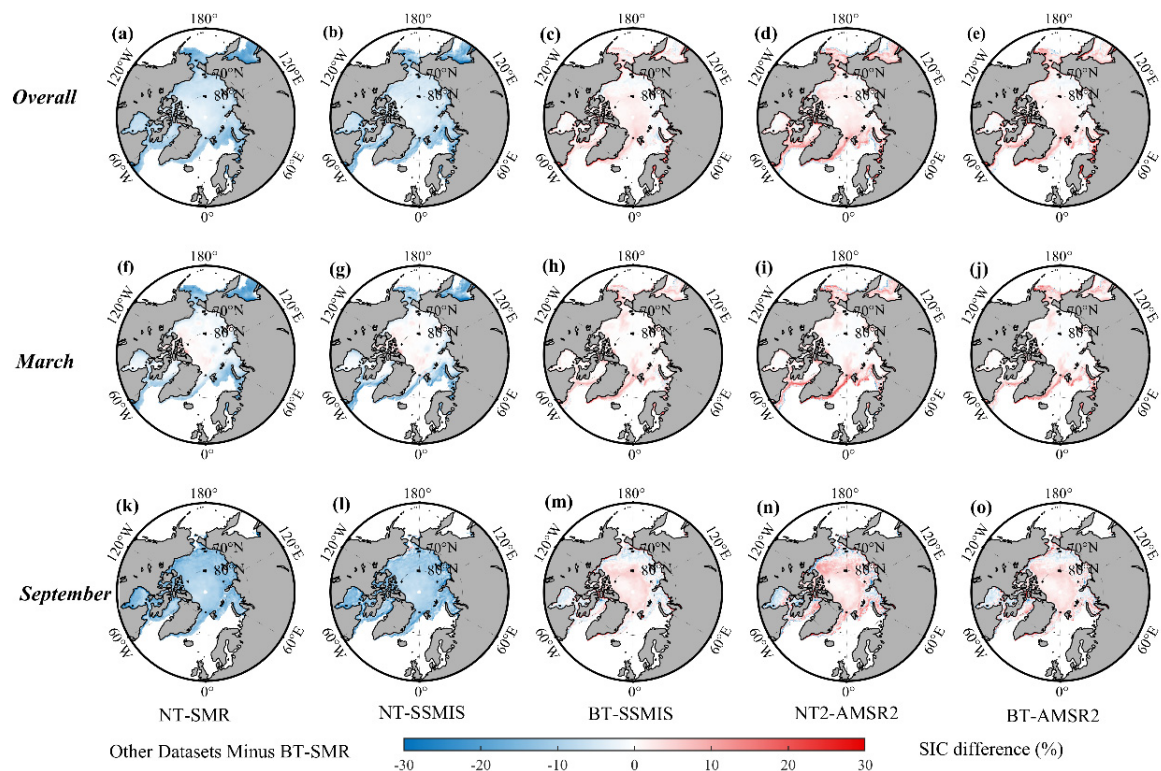

Figure 8. Maps of the overall Arctic difference (**a**–**e**) between five SIC datasets and BT-SMR from January 2019 to December 2021, as well as the months of March (**f**–**j**) and September (**k**–**o**). Grey indicates land, red indicates positive deviations, and blue indicates negative deviations.

Table 4. Parameters for assessing Arctic SIC differences between different SIC datasets and BT-SMR. Bias is the mean difference PM SIC minus BT-SMR SIC, and MAE is the mean absolute error. RMSE is the root mean square error, and R^2 is the squared linear correlation coefficient. All concentration values are given as percentages.

	ID	NT-SMR	NT-SSMIS	BT-SSMIS	NT2-AMSR	BT-AMSR
Overall	Bias	−8.87	−7.96	2.89	3.26	3.25
	MAE	9.00	8.20	3.64	4.71	4.16
	RMSE	10.59	10.35	6.74	7.55	7.48
	R^2	0.97	0.96	0.96	0.95	0.95
March	Bias	−5.38	−4.68	2.01	2.06	2.11
	MAE	5.87	5.36	2.33	3.44	2.77
	RMSE	8.71	8.50	4.09	5.92	5.13
	R^2	0.97	0.97	0.98	0.96	0.97
September	Bias	−11.91	−11.34	1.98	2.14	2.18
	MAE	12.12	11.57	4.43	6.06	4.86
	RMSE	13.21	12.96	8.21	9.08	8.37
	R^2	0.96	0.95	0.91	0.90	0.91

4.2.2. Antarctic SIC and Spatial Distribution Differences

Similar to the Arctic, the six SIC products have similar interannual trends, but the differences among the products were larger than those in the Arctic, as shown in Figure 9a. In winter, the values of daily average SIC were relatively stable, mainly in the range of 75–95%, with NT2-AMSR2 being the largest at ~95% and NT-SMR and NT-SSMIS products being the smallest at ~75–80%. The BT-SMR results obtained in this study were slightly higher than those of BT-SSMIS and BT-AMSR2, with approximately 85–90%. As the sea ice in the Antarctic mainly consists of first-year ice, the daily average SIC is significantly different in November–April, the difference increases significantly, and the values of daily SIC are concentrated primarily in the range of 60–80%. The NT2-AMSR2 inversion results are the largest at approximately 90%; the NT-SMR and NT-SSMIS inversion results are the smallest at approximately 65–75%, the inversion results based on the BT algorithm are between those of the NT2 and NT algorithms at approximately 70–80%, and the difference peaks around March each year. Overall, the SIC variation based on different sensors using the same algorithm is less than 5%, with a more consistent interannual variability trend. SIC variation based on different algorithms that use the same sensor is less than 10%, and the SIC obtained by the NT2 algorithm is up to 25% higher than the SIC produced by the NT algorithm. For the BT algorithm, the three-year trend shows that the BT-SMR in summer is slightly smaller than the BT-SSMIS and BT-AMSR2, and that the BT-SMR in the winter is slightly larger than these two algorithms. Simultaneously, all algorithms reveal that the daily average SIC in summer 2021 in the Antarctic was smaller than that in the previous two years, which may be associated with a warming climate and accelerated melting of sea ice.
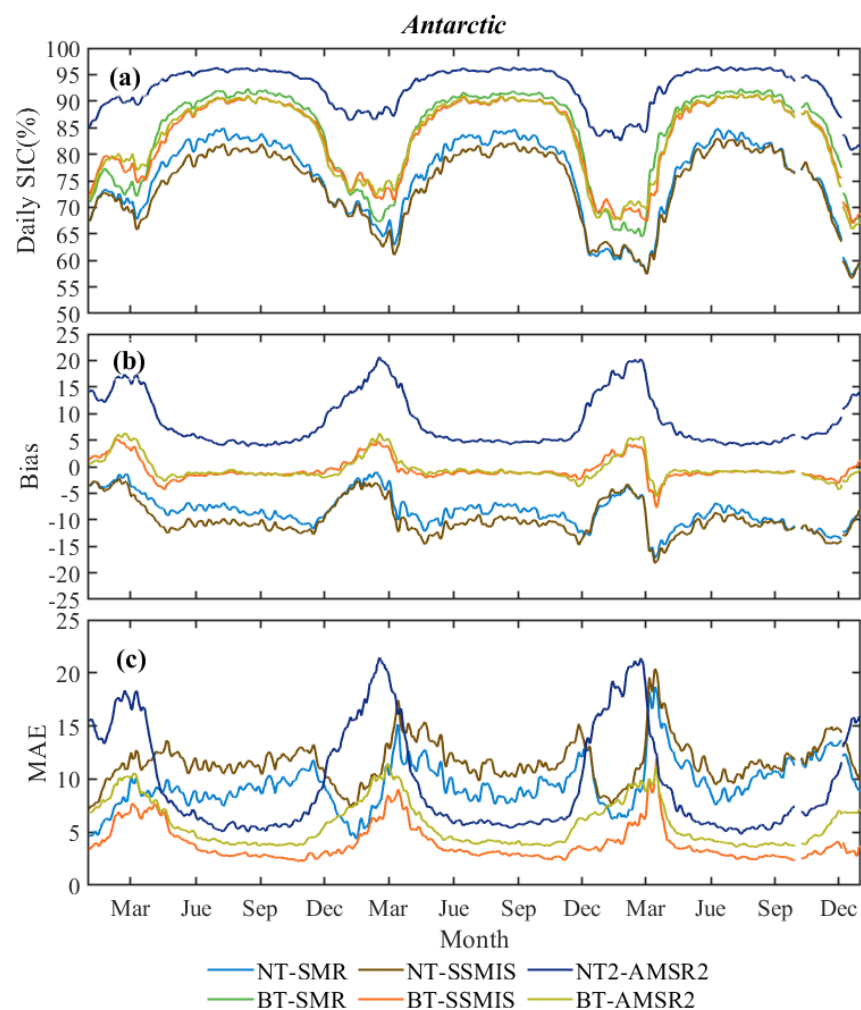

Figure 9. Same as in Figure 7 but in the Antarctic.

The differences between different SIC products and BT-SMR can be seen more clearly based on the bias (Figure 9b) and MAE (Figure 9c) time series plots between different SIC products and BT-SMR. The five SIC products can be classified into three categories based on the bias metric, the first being NT-AMSR2, which exhibits an absolute positive deviation from BT-SMR with an overall bias of 5.17%. The second category was BT-SSMIS and BT-AMSR2, which showed less than 1% bias with BT-SMR in winter and a positive bias of less than 5% in November–April, with overall biases of −0.75 and −0.12, respectively. The third category was NT-SMR and NT-SSMIS, which showed a negative bias of less than 10% with BT-SMR in winter and less than 5% in November–April, and NT-SMR was better than NT-SSMIS, with overall biases of −8.11 and −10.89 for both products, respectively. In terms of MAE parameters, the overall MAEs between NT-SSMIS, NT-SSMIS, BT-SSMIS, BT-AMSR2, and NT2-AMSR2 and BT-SMR were 8.25, 11.03, 1.93, 5.81, and 2.50, respectively. As a result, the BT-SSMIS and BT-SMR products in the Antarctic had the smallest differences, while the NT-SSMIS and BT-SMR products had the most significant differences.

The same method was applied to the spatial and temporal distribution of the difference in Antarctic SIC. We selected the months of September and March in winter and summer, respectively, to plot the difference in the spatial and temporal distributions of different SIC products compared to BT-SMR, as shown in Figure 10. The differences in daily average SIC during March and September are shown in Figure 10f–o, and the detailed statistical parameters are shown in Table 5. In the overall spatial distribution, NT-SMR and NT-SSMIS revealed more significant differences in the high-concentration ice area and relatively more minor differences in MIZ, indicating an overall negative deviation. BT-SSMIS and BT-AMSR2 showed a slightly negative deviation in the high-concentration ice area and a slightly positive deviation in the MIZ. However, NT2-ASMR2 showed an overall positive deviation, and the positive differences in MIZ were more extensive than those in the high-concentration ice area. During March, when it is late summer in the Antarctic and the SIE is at its minimum, NT-SMR and NT-SSMIS showed a negative deviation in most areas but a slightly positive deviation in the Antarctic Peninsula and Princess Astrid Coast. BT-SSMIS and BT-AMSR2 were similar to the NT-based algorithm, exhibiting a negative deviation in most areas and a slightly positive deviation in the Antarctic Peninsula, Amundsen Sea, and Princess Astrid Coast. However, NT2-AMSR2 showed a positive deviation in almost all areas, with the most significant positive deviation in the Weddell Sea near the border with the Antarctic Peninsula and the Amundsen Sea. In September, when it is late winter in the Antarctic and the SIE reaches its maximum, NT-SMR and NT-SSMIS exhibited negative deviations, with NT-SSMIS showing the most extensive negative deviation of approximately −10.51. BT-SSMIS and BT-AMSR2 differed by less than 1%. The deviation was negative in the high-SIC ice regions and positive in the MIZ, with BT-AMSR2 showing the slightest deviation of approximately −0.24, mainly due to the mutual offset of positive and negative deviations. NT2-AMSR2 showed a positive deviation, with the most significant positive deviation in the MIZ and a relatively small deviation in the high-SIC ice regions. According to the MAE and RMSE parameters of Table 5, the overall average, March average, and September average show that the difference between BT-SSMIS and BT-SSMIS was the most negligible, the negative difference between NT1-SSMIS and BT-SMR was the largest, and the positive difference between NT2-AMSR2 and BT-SMR was the largest. The assessment of the September average was better than the overall average and better than the March average.
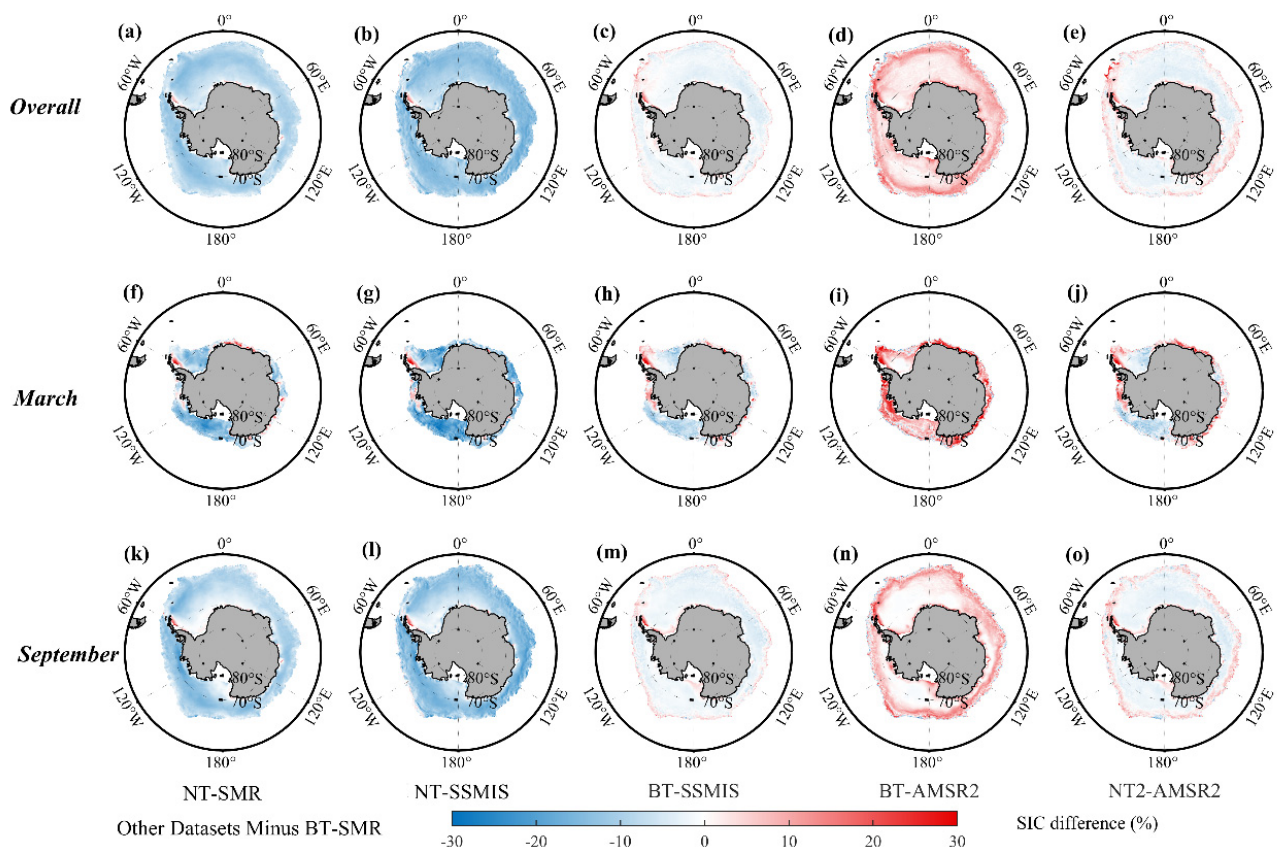
Figure 10. Same as in Figure 8 but in the Antarctic.

Table 5. Same as in Table 4 but in the Antarctic.

	ID	NT-SMR	NT-SSMIS	BT-SSMIS	NT2-AMSR	BT-AMSR
Overall	Bias	−8.11	−10.89	−0.75	5.17	−0.12
	MAE	8.25	11.03	1.93	5.81	2.50
	RMSE	8.79	11.61	2.64	7.22	3.62
	R^2	0.99	0.98	0.99	0.97	0.99
March	Bias	−7.86	−12.43	−1.88	9.23	0.68
	MAE	9.97	13.84	5.83	10.72	6.66
	RMSE	11.65	15.53	7.61	13.66	8.92
	R^2	0.91	0.90	0.93	0.89	0.90
September	Bias	−7.74	−10.51	0.96	4.22	−0.24
	MAE	7.95	10.72	2.23	4.95	2.67
	RMSE	8.94	11.72	2.95	7.04	3.65
	R^2	0.98	0.97	0.99	0.97	0.99

4.2.3. Assessing SIC Differences by Intervals

Whether in the Antarctic or the Arctic (Figure 11a–f), the SIC difference was the slightest in the high-SIC (70–100%) regions and most extensive in the medium-SIC (70–100%) regions. In the Arctic SIC (70–100%) region, BT-SSMIS, NT2-AMSR, and BT-AMSR2 had positive deviations from BT-SMR with biases of 2.70, 2.75, and 2.25 and MAEs of 3.17, 4.31, and 3.72, respectively. NT-SMR and NT-SSMIS showed negative deviations from BT-SMR, with NT-SMR having the most considerable negative differences for bias and MAE at −6.63 and −7.31, respectively. In the Antarctic SIC (70–100%) region, only the NT2-AMSR2 and BT-SMR products showed positive deviations, with BIAS and MAE values of 5.02 and 6.61, respectively. NT-SSMIS, BT-SSMIS, and BT-AMSR2 all showed negative deviations from BT-SMR, with SSMIS showing the slightest negative deviation and NT-SSMIS showing the

largest. The NT-SMR, NT-SSMIS, BT-SSMIS, and BT-AMSR2 products had a more significant bias and MAE than Antarctic SIC (15–30%) and medium SIC (70–100%), with only NT-AMSR2 being slightly smaller than Antarctic SIC (15–30%) and medium SIC (70–100%). Overall, the difference between Arctic SIC products and BT-SMR was greater than that of the Antarctic. The difference in the assessment parameters between products in the high-SIC regions was more significant than those in the low- and medium-SIC regions.
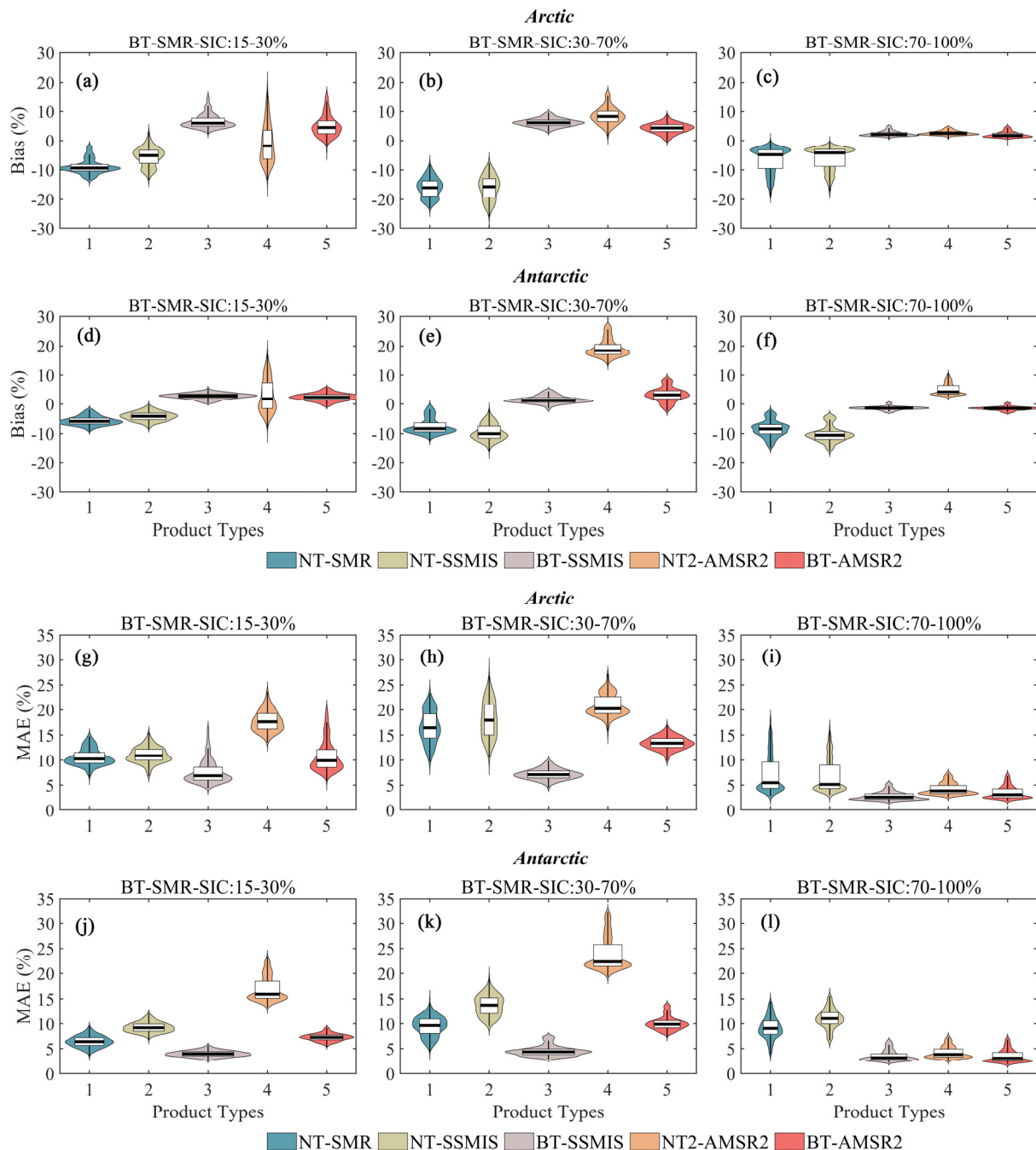

Figure 11. Violin chart of SIC differences between the five different SIC products and BT-SMR SIC with BT-SMR SICs of 15–30%, 30–70%, and 70–100% from January 2019 to December 2021. The x-axis denotes different SIC products; (**a–f**) the y-axis denotes bias; (**g–l**) the y-axis denotes the mean absolute error; the first and third rows of the diagram depict the Arctic, and the second and fourth rows depict the Antarctic.

4.3. Inter-Comparison of the Ship-Based SIC

In this Subsection, we compare and evaluate six SIC products based on ship-based visualization data. Ship-based observations of manual sea ice cover conditions have their limitations. The observation values are collected by numerous observers with different experiences during vessel movement, making it quite challenging to evaluate the sea ice cover as 50% or 60% of the 1 km radius area around the ship. As a result, the estimation accuracy for ship-board moderate SIC (30–70%) is further reduced [31], which has significant implications for evaluating SIC at different spatial resolutions. Worby and Comiso [47] analyzed sea ice observations from different observers for the same scenario and derived approximately 5–10% uncertainty estimates for the overall SIC.

Ship-based observations are often used as essential truth data to evaluate the SIC products acquired by satellite-based microwave radiometers. It was necessary to evaluate bootstrap SIC values using ship-based observations since they were applied to the HY2B SMR sensor for the first time.

4.3.1. Arctic

For the Arctic, all six SIC products compare well with ship-based data (Figure 12). For the high-SIC (70–100%) regions, NT-SMR and NT-SSMIS show asymmetric distributions, with a significant fraction of satellite SIC below 60%, which implies that the negative differences between the NT-based SIC products and ship-based SIC are larger than other products; BT-SMR shows the best symmetric distribution; BT-SSMIS, BT-AMSR2, and NT2-AMSR2 all show asymmetric distributions, with all three products slightly overestimating ship-based observations and NT2-AMSR2 overestimating ship-based observations the most. According to the red fitted curve, BT-SMR is closer to ship-based observations than the other five products in moderate SIC (30–70%). Out of the six SIC products, the overall deviation of NT-SMR, BT-SMR, and NT-SSMIS was negative, with the largest negative deviation of NT-SSMIS being approximately −9.42% and the smallest negative deviation of BT-SMR being approximately −0.70%. The overall deviation of BT-SSMIS, BT-AMSR2, and NT2-AMSR2 was positive, and the maximum positive deviation of NT2-AMSR2 was approximately 5.53%. Overall, among the PM SIC products, the ship-based SIC matches well in the high SIC regions, and NT-SMR and NT-SSMIS tend to underestimate the ship-based SIC in the low SIC regions; BT-SSMIS, NT2-AMSR2, and BT-AMSR2 significantly overestimate the ship-based SIC, and BT-SMR matches best with ship-based observations in the medium SIC regions. Moreover, BT-AMSR2 has the highest correlation with ship-based SIC; however, the slope of the BT-SMR fitted curve is closer to the 1:1 identification line, which is consistent with the assessment of Kern et al. [31], who used ship-based observations.

In addition to the evaluation of the overall data, winter (November–April) and summer (May–October) parameters were also calculated, and the values are shown in Table 6. For the three different types of assessments, the highest correlation was found in winter. The winter and summer data accounted for 40.54% and 49.46% of the overall Arctic data, respectively, representing a uniform and representative distribution. BT-SMR had the lowest bias and MAE (−0.39% and 4.87%, respectively), while NT-SSMIS had the most remarkable differences (−8.04% and 9.76%) from ship-based SIC in winter. In summer, BT-SMR deviated from ship-based SIC the least, by approximately −0.91%. Generally, SIC products based on the BT algorithm are superior to those based on the NT and NT2 algorithms. The MAEs of different SIC products increase by approximately 5% in summer compared to winter, which means that PM-based SIC has better accuracy in winter. This result is mainly due to the high sensitivity of microwaves to atmospheric conditions and sea ice surface melting.
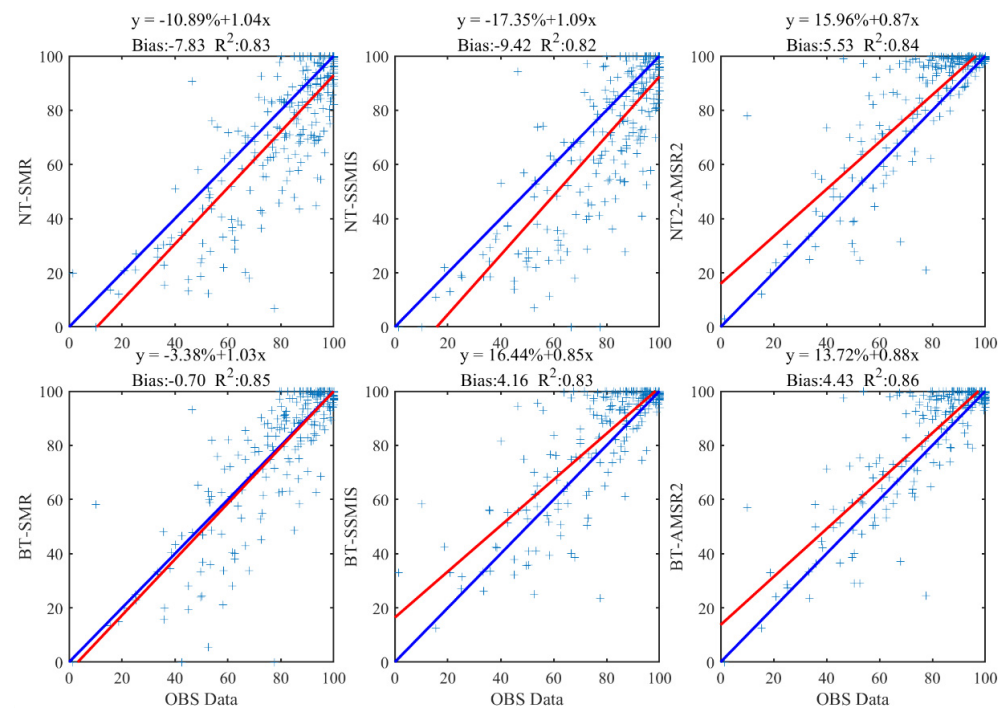
Figure 12. Scatterplots of co-located daily average SIC from visual ship-based observations (Ice Watch/ASSIST, x-axis) and the six satellite SIC algorithm products (y-axes) for the Arctic during 2019–2021. The blue solid lines denote the identity line. The red solid lines denote the linear regression of the respective value pairs. The linear regression equation, bias, and squared linear correlation coefficient (R^2) are given at the top of every image.

Table 6. Summary of statistics of the comparison between daily average ship-based and PM SIC data for the entire year, only winter, and only summer.

	ID	NT-SMR	BT-SMR	NT-SSMIS	BT-SSMIS	NT2-AMSR	BT-AMSR
Overall	Bias	−7.83	−0.70	−9.42	4.16	5.53	4.43
	MAE	11.23	8.53	12.72	8.69	8.47	7.99
	RMSE	16.06	13.12	18.46	12.71	12.87	11.73
	R^2	0.83	0.85	0.82	0.83	0.84	0.86
Winter	Bias	−6.39	−0.39	−8.04	1.17	6.52	1.83
	MAE	7.96	4.87	9.76	5.23	5.44	5.07
	RMSE	12.17	7.41	15.02	7.74	7.97	7.12
	R^2	0.85	0.90	0.84	0.89	0.90	0.91
Summer	Bias	−8.80	−0.91	−10.36	6.19	6.90	6.20
	MAE	13.46	11.02	14.72	11.06	10.53	9.99
	RMSE	18.24	15.87	20.46	15.19	15.34	14.04
	R^2	0.80	0.82	0.78	0.80	0.81	0.84

A heatmap diagram was drawn to illustrate the differences between the PM SIC and the ship-based SIC, as shown in Figure 13a. Most differences between the PM SIC and the ship-based SIC are between −20% and 20%. In the Arctic, BT-SMR, BT-SSMIS, and BT-AMSR2 differed from ship-based SIC in the range of [−20%, 20%], accounting for 89%, 90%, and 92% of the total number of samples, respectively; NT2-AMSR2 also accounted for a 90% proportion; and NT-SSMIS accounted for a 75% proportion. Overall, three types of SIC products based on the BT algorithm have higher accuracy, and SIC products based on the NT algorithm tend to underestimate SIC.
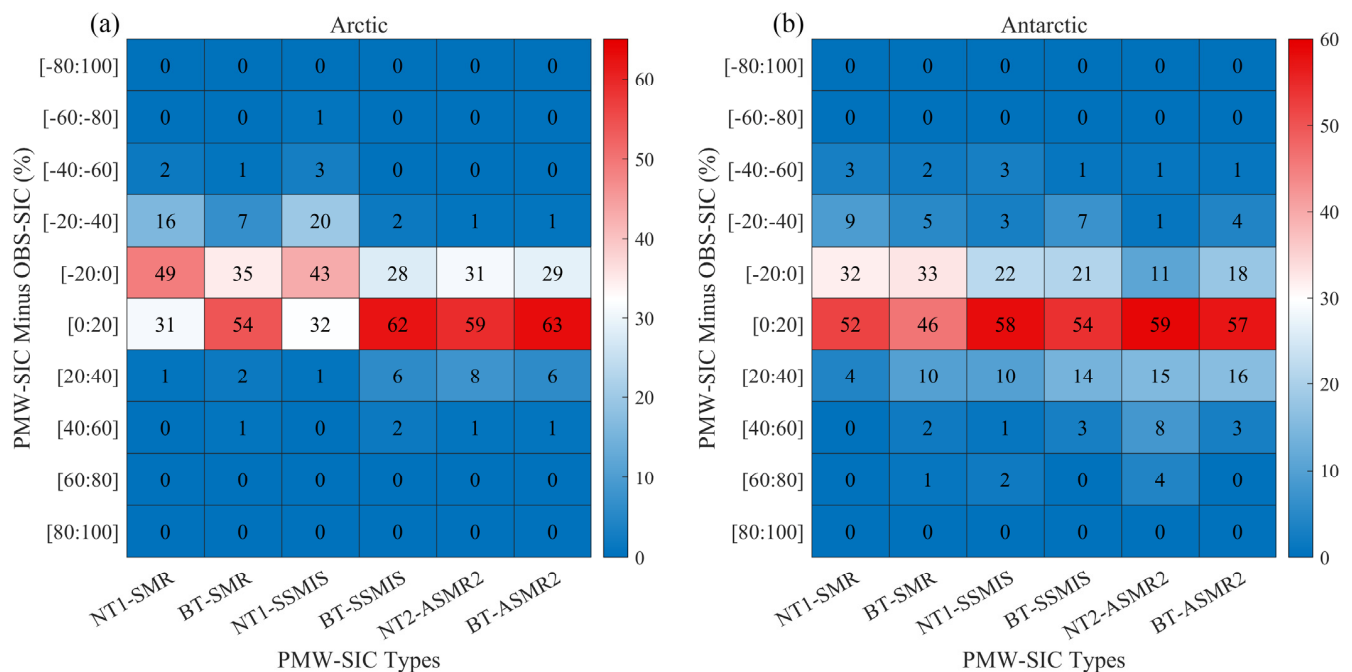
Figure 13. SIC differences between the PM SIC products and ship-based SIC. The number in the grid denotes the proportion of data pairs for the PM SIC products. The horizontal axes denote six different PM SICs. The SIC differences are grouped with an interval of 20% from −100% to 100% (vertical axis). The (**a**) diagram indicates the Arctic and the (**b**) diagram indicates the Antarctic.

4.3.2. Antarctic

In Antarctica, the scatter plots of PM SIC and ship-based SIC along the ship's trajectory are shown in Figure 14. In the high SIC (70–100%) region, all five products show symmetrical distributions, except NT2-AMSR2. NT-SMR and BT-SMR show slightly negative deviations. NT-SSMIS, BT-SSMIS, and BT-AMSR2 show slightly positive deviations, but NT2-AMSR2 is significantly higher than ship-based SIC, with almost no points below the 1:1 identification line. For the moderate SIC (30–70%), BT-SMR is closest to the shipboard observations, except for NT-SMR, which exhibits an overall positive deviation, and the NT2-AMSR2 overestimation is the largest. Overall, the slope of the linear regression fitted curve for SIC products based on the BT algorithm is closer to 1, and the slope of the linear regression fitted curve for NT2-AMSR2 is the largest. NT-SMR shows a negative deviation of approximately −3.75%, NT2-AMSR2 has the largest negative deviation of approximately 14.25%, and BT-SMR has the smallest deviation of approximately 1.42%. We also obtained the parameter statistics in winter (May–October) and summer (November–April), and the corresponding values are shown in Table 7. The table also shows that the deviations of NT-SMR and NT-SSMIS decrease in winter compared to the overall data, and the deviations of the remaining four products increase accordingly and are positive. The MAE and RMSE become smaller for all five products except BT-SMR, and the main reason for this difference is the relatively small sample size of the winter data, which accounts for only 16% of the overall Antarctic sample sizes. The bias of BT-SMR decreases to −0.15% in summer compared to the winter data and decreases accordingly for all products except NT-SMR and NT-SSMIS. In terms of the RMSE parameters, the SIC products increased by approximately 4–6% in summer compared to winter. The correlation coefficients for the different products are higher in summer than in winter, mainly because summer samples account for most of the overall sample, approximately 84%. Overall, the difference between the SMR-based SIC products and ship-based observations is the smallest, and the BT-SMR and ship-based SIC are negligible in summer. The difference between SIC products and ship-based SIC is greater in the Antarctic than in the Arctic, and NT2-AMSR2 shows an overestimation with a larger magnitude in both the Antarctic and the Arctic.
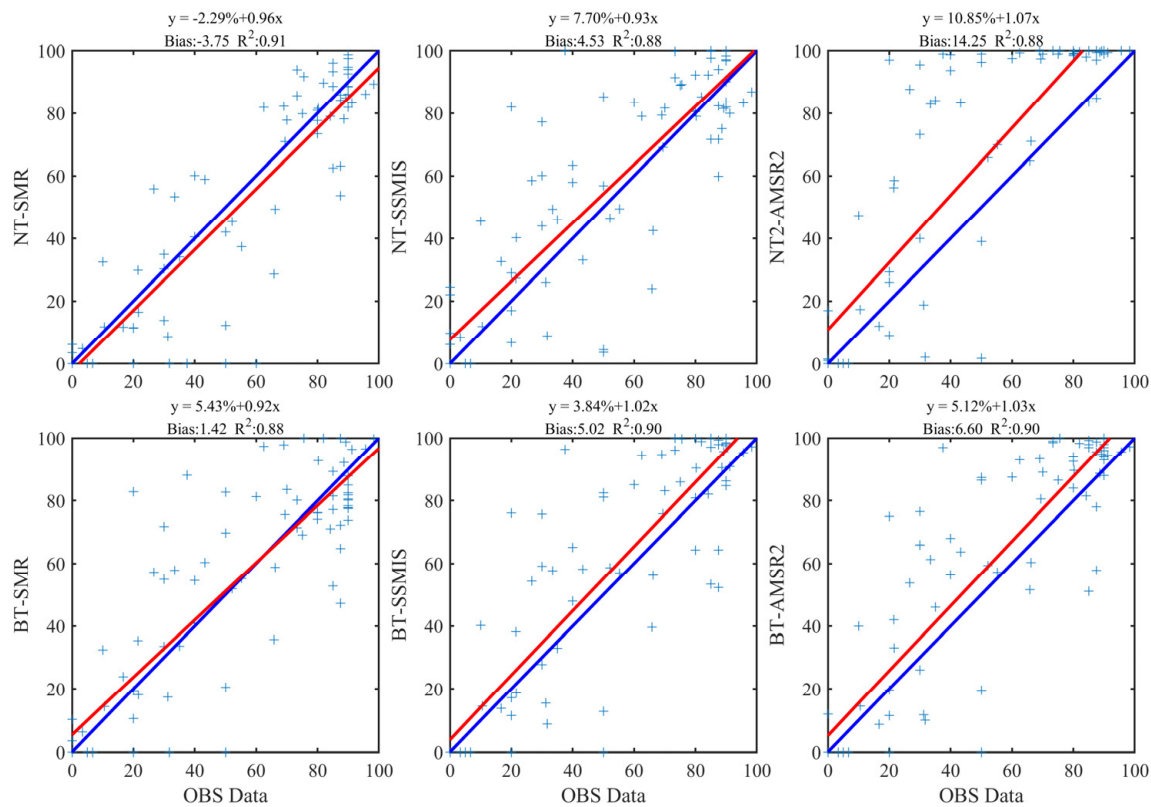
Figure 14. Same as in Figure 12 but in the Antarctic.

Table 7. Same as in Table 6 but in the Antarctic.

	ID	NT-SMR	BT-SMR	NT-SSMIS	BT-SSMIS	NT2-AMSR	BT-AMSR
Overall	Bias	−3.75	1.42	4.53	5.02	14.25	6.60
	MAE	10.13	11.56	12.65	12.43	17.26	12.68
	RMSE	16.12	17.64	18.53	18.46	25.21	18.64
	R^2	0.91	0.88	0.88	0.90	0.88	0.90
Winter	Bias	0.93	11.79	−1.99	10.72	17.01	11.08
	MAE	8.96	13.08	9.30	12.64	17.00	12.27
	RMSE	10.80	17.02	11.35	15.89	20.12	15.41
	R^2	0.71	0.68	0.68	0.66	0.64	0.69
Summer	Bias	−4.47	−0.15	5.52	4.15	13.83	5.92
	MAE	10.32	11.33	13.16	12.39	17.31	12.74
	RMSE	16.78	17.74	19.39	18.82	25.89	19.08
	R^2	0.90	0.87	0.87	0.89	0.87	0.90

Similar to the Arctic, a heat map was created representing the difference between PM SIC and ship-based SIC, as shown in Figure 13b. The difference between PM SIC and ship-based SIC was overwhelming, within [−20%, 20%], and NT2-AMSR2 was within [40–80%] for approximately 13% of the total samples. In contrast to the Arctic, the SIC products based on the NT algorithm tend to overestimate the SIC values, which may be related to the size of the Antarctic sample selected for this study. In the Antarctic, the differences were located within the [0%, 20%] interval, which is significantly higher than [−20%, 0%]. BT-SMR, BT-SSMIS, and BT-AMSR2 differed from ship-based SIC in the [−20%, 20%] interval, accounting for 87%, 82%, and 82% of the overall Antarctic sample size, respectively, which was smaller than that of the Arctic. Generally, the difference between satellite-based SIC products and ship-based observations is greater in the Antarctic than that in the Arctic.

The scale differences and observational limitations between ship-based and satellite-based sea ice concentration observations are noteworthy, and the variability in ship-based observations depends significantly on the proportion of thin ice [29]. The spatial and temporal distribution of SIC values is limited by the small Antarctic shipboard observations collected for 2019–2021; thus, the results of the accuracy validation are to be further evaluated. In the Antarctic, sea ice is dominated by first-year ice. In future works, we will assess the stages of sea ice during the melting period based on MODIS (Moderate Resolution Imaging Spectroradiometer) or SAR (Sentinel-1A) data, and also evaluate the accuracy of BT-SMR results obtained in this study in MIZ.

5. Discussion

5.1. Arctic SIE and SIA Time Series Analysis

The time series of Arctic SIE (Figure 15a) and SIA (Figure 15b) from 2019 to 2021 reveal consistent trends, with the March SIE and SIA reaching maximum values and the September SIE and SIA reaching minimum values. The maximum and minimum values of SIE for the ASI-AMSR2 products are 14.497×10^6 km^2 and 3.385×10^6 km^2, respectively; the maximum and minimum values of SIA are 13.565×10^6 km^2 and 2.900×10^6 km^2, respectively. The SIE and SIA of the six SIC products with 25 km spatial resolutions are smaller than those of the ASI-AMSR2 products, but the differences in SIE with the exact spatial resolution of 25 km are minor. The missing data near the North Pole due to satellite orbit inclination and width of the swath were filled with a constant SIC = 98%, and the fixed value used in this study is consistent with the value used by Kern et al. [31]. Andersen et al. [51] compared passive microwave SIC with SAR observations in winter at high latitudes and found an average SIC of approximately 98%, with a slightly smaller value of approximately 95% in summer. In summer, a fixed value of 98% instead of 95% would tend to overestimate the SIA by approximately 1×10^4 km^2. However, this difference seems negligible compared to the other factors that contribute to the difference. Time series plots are shown in Figure 15b,d, demonstrating the differences in SIE and SIA between different SIC products and BT-SMR. The SIE difference between ASI-AMSR2 and BT-SMR is larger at approximately 0.385×10^6 km^2; the SIE difference between other 25 km SIC products and BT-SMR is less than 0.05×10^6 km^2. The difference in SIEs between BT-SSMIS and BT-SMR is the smallest. The negative difference between NT-SSMIS and BT-SMR is the largest, at approximately -0.047×10^6 km^2, which means that products with 25 km spatial resolutions can monitor whether there is extensive sea ice in the image grid. The difference is mainly reflected in SIC values, which can be better reflected in SIA. ASI-AMSR2 shows the most considerable positive difference in SIA with BT-SMR at approximately 0.359×10^6 km^2, followed by NT2-AMSR2 with 0.313×10^6 km^2. The SIA difference between NT-SMR and BT-SMR is the largest at approximately -0.535×10^6 km^2; the SIA difference between BT-AMSR2 and BT-SMR is the smallest at approximately 0.210×10^6 km^2.
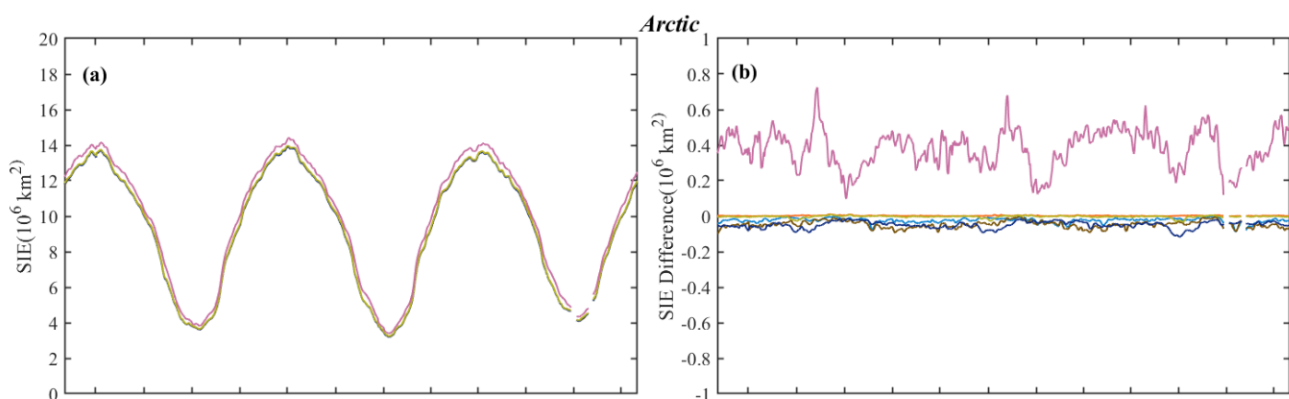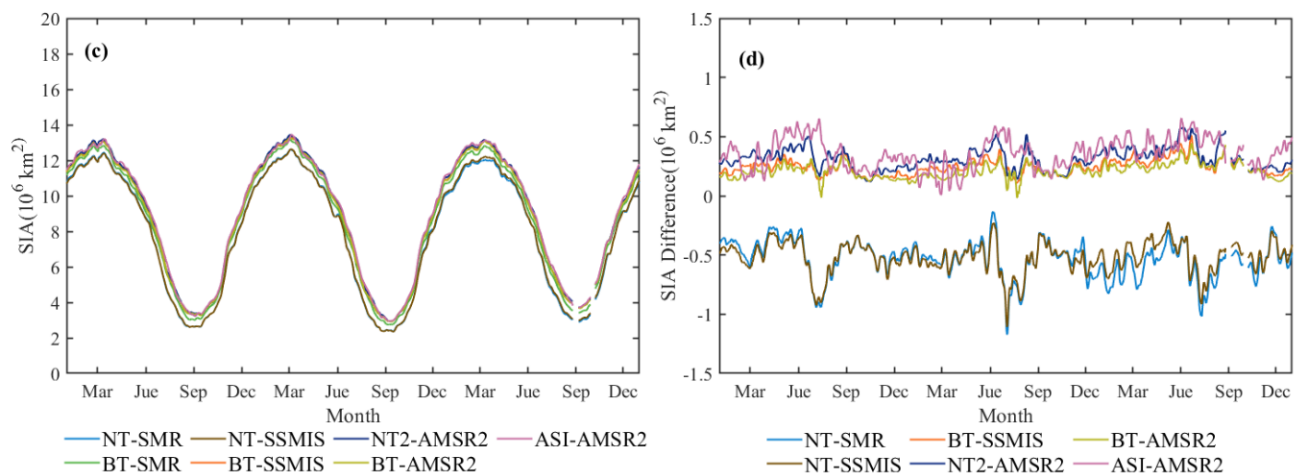

Figure 15. *Cont.*

Figure 15. Arctic SIE (**a**) and SIE difference (**b**), and SIA (**c**) and SIA difference (**d**) time series from the SIC datasets used.

5.2. Antarctic SIE and SIA Time Series Analysis

The Antarctic SIE and SIA time series from 2019 to 2021 show similar trends to those of the Arctic. The SIA and SIE reach their minimums in March for the Antarctic and their maximums in September. For the SIE, the ASI-AMSR2 product has the largest value of $\sim$19.33 $\times$ 10^6 km^2 and the NT-SSMIS product has the smallest value of approximately 1.93 $\times$ 10^6 km^2. As shown in Figure 16b, SIE differences between different products and BT-SMR are shown in the graph. The difference in SIE products for all 25 km spatial resolutions is small at $\sim$$-0.1$ $\times$ 10^6 km^2, and the SIE of ASI-AMSR2 products shows a positive deviation from BT-SMR in winter at approximately 0.2 to 0.3 $\times$ 10^6 km^2. In summer (December–March), the ASI-AMSR2 SIE shows a negative deviation of approximately -0.2 $\times$ 10^6 km^2. However, in 2020 and 2021, the negative variance is as high as -0.6 to -0.8 $\times$ 10^6 km^2. For SIA, the NT2-AMSR2 product has the largest value of approximately 18.31 $\times$ 10^6 km^2; NT-SSMIS has the smallest value of $\sim$1.33 $\times$ 10^6 km^2; the difference between different products and BT-SMR SIA is shown in Figure 16d with seasonal variation tendency. The positive deviation between NT2-AMSR2 and BT-SMR is the largest at approximately 0.5 $\times$ 10^6 km^2 in winter and 1.0 $\times$ 10^6 km^2 in summer. The difference between ASI-AMSR2 and BT-SMR is $\sim$0.4 $\times$ 10^6 km^2 in winter and nearly negligible in summer. The difference between BT-SSMIS and BT-AMSR2 and BT-SMR SIA is always less than 0.2 $\times$ 10^6 km^2. The positive deviation in January–March is mainly due to the slightly larger BT-SSMIS and BT-AMSR2 SIC than BT-SMR SIC. Nevertheless, the difference is almost zero in April–October, resulting from the offset positive and negative differences in SIC values. The NT-SMR and NT-SSMIS differences from BT-SMR SIA are negative, and the maximum negative difference is up to -2.0 $\times$ 10^6 km^2. At the end of summer, the difference is relatively stable around March each year, and the negative difference increases from March to December, and decreases from December to February, with interannual variation characteristics, where the difference between NT-SMR and BT-SMR is smaller than that of NT-SSMIS.
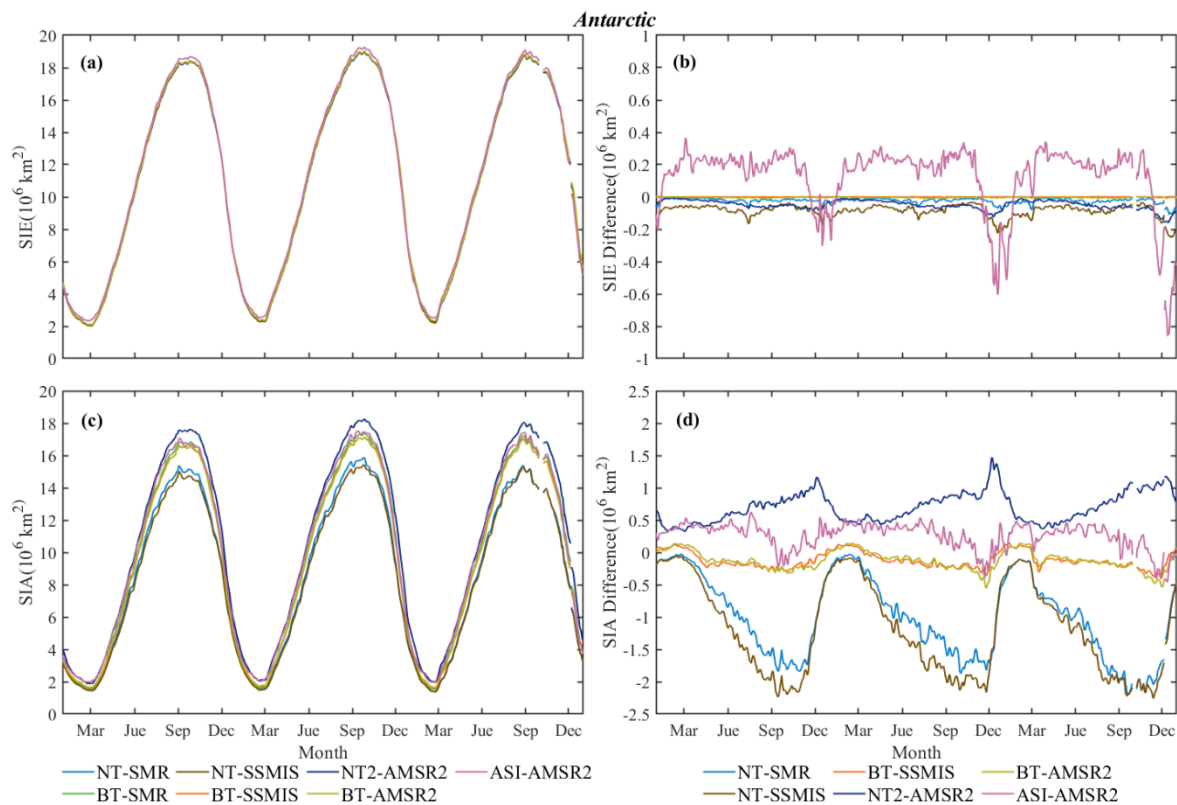
Figure 16. Same as in Figure 15 but in the Antarctic.

5.3. Assessing MIZ SIE with Different BT SIC Products

The differences between the different BT SIC products in the MIZ SIE are shown in Figure 17. The MAE of the MIZ SIE of BT-SMR and BT-SSMIS increases by 0.19×10^6 km^2 for the Arctic and Antarctic compared to the total SIE. For both BT-SMR and BT-AMSR2, the increase in MAE of the MIZ SIE is 0.12×10^6 km^2, indicating a more significant difference in PM SIC in the MIZ compared to the overall sea area. This study identified the region with SIC < 70% as the marginal ice zone. In the Arctic, the BT-SMR MIZ SIE is higher than the BT-SSMIS MIZ SIE and BT-AMSR2 MIZ SIE, which is mainly caused by the BT-SMR underestimating the BT-SSMIS and BT-AMSR2 SIC values, with the BT-SMR classifying more pixels as marginal ice areas. The MIZ SIE of the three products accounted for approximately 5% of the total SIE, but with the increase in temperature and melting pool, it peaked in August at approximately 20% of the total SIE, with MAEs of BT-SMR, BT-SSMIS, and BT-AMSR2 MIZ SIE fractions of 2.50% and 2.56%, respectively. In the Antarctic, the PM MIZ SIE is approximately 0.95~3.7 $\times 10^6$ km^2, which is significantly larger than that in the Arctic, mainly because the sea ice type in the Antarctic is dominated by first-year ice. Compared with the BT-SSMIS MIZ SIE, the BT-SMR MIZ SIE is closer to the BT-AMSR2 MIZ SIE, with a difference of 0.10×10^6 km^2. However, the BT-SMR MIZ SIE was lower during the Antarctic August–December summer period, possibly due to partially overestimating BT-SMR during the summer period. Regarding the MIZ SIE fraction, the proportion of SIE for the three SIC products is approximately 10% in winter, and the proportion of SIE is larger during the summer period, accounting for nearly 50% of the overall SIE in the maximum period. The MAEs between the BT-SMR MIZ SIE fraction and BT-SSMIS MIZ SIE fraction, and the BT-AMSR2 MIZ SIE fraction, are 1.70% and 1.59%, respectively. In general, the differences between BT-SMR and BT-SSMIS MIZ SIE are smaller in the Arctic, and the differences between BT-SMR and BT-AMSR2 MIZ SIE are relatively slight in the Antarctic. The three SIC products based on the bootstrap algorithm show consistent performances for the MIZ SIE, and their variations have seasonal characteristics. In winter, the MIZ SIE is relatively small and accounts for a small proportion of the total

SIE. However, as the temperature rises, the MIZ SIE increases rapidly, and the proportion gradually increases. The Antarctic is dominated by first-year ice, so the SIE and SIE fraction increase much faster than in the Arctic.
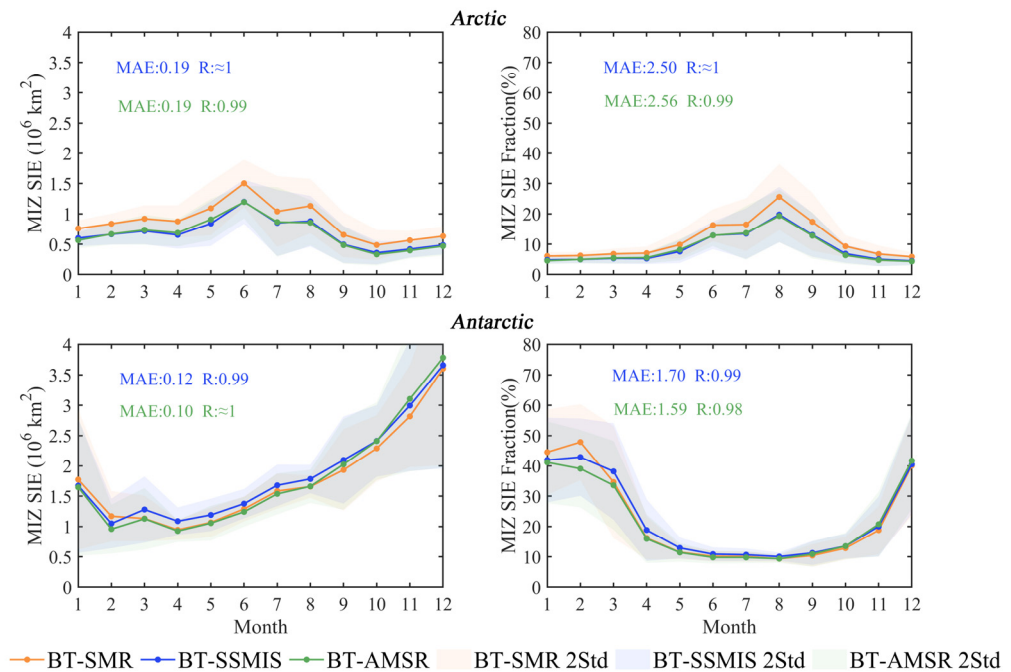

Figure 17. Monthly MIZ SIE and MIZ SIE fraction during 2019–2021. Additionally, the differences in MIZ SIE and MIZ SIE fraction between the BT-SMR and BT-SSMIS (blue number) and between the BT-SMR and BT-AMSR2 (green number) are shown. The shading presents the 2 STDs from the monthly MIZ SIE and MIZ SIE fraction.

6. Conclusions

In this study, the SIC retrieval method based on the T_B data of HY-2B SMR was applied to the dynamic tie-points from an improved bootstrap algorithm. The SIC products of the Arctic and Antarctic during 2019–2021 of the established method were compared with the published similar datasets and evaluated with the ship-based observations. BT-SMR products present the similar interannual trends as the other products for the Arctic and Antarctic. BT-SMR and BT-SSMIS from NSIDC showed the slightest difference, with MAE of 3.64% in the Arctic and 1.93% in the Antarctic. Comparison of the six 25 km SIC products with ship-based observations reveals that the correlation coefficient between BT-SMR and ship-based SIC is 0.85 in the Arctic, and the slope of the fitted curve is close to the 1:1 identification line.

In summary, the BT algorithm was first applied to SMR T_B data of HY-2B. The overall performance was satisfactory, but the difference between other SIC products and similar BT-based SIC products in the summer was relatively larger. Therefore, subsequent work will thoroughly analyze the reasons for this difference. The T_B data used in this paper are not cross-calibrated with the SSMIS and AMSR2 sensors. The calibrated T_B data will be used in subsequent work to optimize the dynamic tie-points and obtain more consistent long-term time series SIC products.

Author Contributions: Conceptualization, S.W.; methodology, S.W., L.S. and Z.D.; writing, S.W.; validation, T.Z. and D.L.; and supervision and funding acquisition, B.Z. and L.S. All authors have read and agreed to the published version of the manuscript.

Data Availability Statement: The HY-2B SMR T_B data can be requested from the website of the National Satellite Ocean Application Service (NSOAS) of China (http://www.nsoas.org.cn/index.html, accessed on 6 December 2022). The NT-SSMIS dataset can be requested from NSIDC (https://nsidc.org/data/NSIDC-0051/versions/1, accessed on 6 December 2022). The BT-SSMIS dataset can be downloaded from NSIDC (https://nsidc.org/data/nsidc-0079/versions/3, accessed on 6 December 2022). The NT2-AMSR2 and BT-AMSR2 data can be requested from NSIDC (https://nsidc.org/data/AU_SI25/versions/1, accessed on 6 December 2022). The ASI-AMSR2 data can be requested from the University of Bremen (https://seaice.uni-bremen.de/data/, accessed on 6 December 2022). The ship-based observation data can be requested from https://www.pangaea.de/, https://icewatch.met.no/, accessed on 6 December 2022. The SIC data retrieved in this study are available upon request from the corresponding author.

Conflicts of Interest: The authors declare that they have no conflict of interest.

References

1. Serreze, M.C.; Barrett, A.P.; Stroeve, J.C.; Kindig, D.N.; Holland, M.M. The emergence of surface-based Arctic amplification. *Cryosphere* **2009**, *3*, 11–19. [CrossRef]
2. Manabe, S.; Wetherald, R.T. The effects of doubling the CO_2 concentration on the climate of a general circulation model. *J. Atmos. Sci.* **1975**, *32*, 3–15. [CrossRef]
3. Ingels, J.; Aronson, R.B.; Smith, C.R.; Baco, A.; Bik, H.M.; Blake, J.A.; Brandt, A.; Cape, M.; Demaster, D.; Dolan, E. Antarctic ecosystem responses following ice-shelf collapse and iceberg calving: Science review and future research. *Wiley Interdiscip. Rev. Clim. Chang.* **2021**, *12*, e682. [CrossRef]
4. Cheung, H.H.; Keenlyside, N.; Omrani, N.-E.; Zhou, W. Remarkable link between projected uncertainties of Arctic sea-ice decline and winter Eurasian climate. *Adv. Atmos. Sci.* **2018**, *35*, 38–51. [CrossRef]
5. Xu, S.; Zhou, L.; Liu, J.; Lu, H.; Wang, B. Data Synergy between Altimetry and L-Band Passive Microwave Remote Sensing for the Retrieval of Sea Ice Parameters—A Theoretical Study of Methodology. *Remote Sens.* **2017**, *9*, 1079. [CrossRef]
6. Kwok, R. Arctic sea ice thickness, volume, and multiyear ice coverage: Losses and coupled variability (1958–2018). *Environ. Res. Lett.* **2018**, *13*, 105005. [CrossRef]
7. Kinnard, C.; Zdanowicz, C.M.; Fisher, D.A.; Isaksson, E.; de Vernal, A.; Thompson, L.G. Reconstructed changes in Arctic sea ice over the past 1450 years. *Nature* **2011**, *479*, 509–512. [CrossRef] [PubMed]
8. Yu, L.; Zhong, S.; Winkler, J.A.; Zhou, M.; Lenschow, D.H.; Li, B.; Wang, X.; Yang, Q. Possible connections of the opposite trends in Arctic and Antarctic sea-ice cover. *Sci. Rep.* **2017**, *7*, 45804. [CrossRef]
9. Stroeve, J.C.; Markus, T.; Boisvert, L.; Miller, J.; Barrett, A. Changes in Arctic melt season and implications for sea ice loss. *Geophys. Res. Lett.* **2014**, *41*, 1216–1225. [CrossRef]
10. Tikhonov, V.; Raev, M.; Sharkov, E.; Boyarskii, D.; Repina, I.; Komarova, N.Y. Satellite microwave radiometry of sea ice of polar regions: A review. *Izv. Atmos. Ocean. Phys.* **2016**, *52*, 1012–1030. [CrossRef]
11. Alekseeva, T.; Tikhonov, V.; Frolov, S.; Repina, I.; Raev, M.; Sokolova, J.; Sharkov, E.; Afanasieva, E.; Serovetnikov, S. Comparison of Arctic Sea Ice concentrations from the NASA team, ASI, and VASIA2 algorithms with summer and winter ship data. *Remote Sens.* **2019**, *11*, 2481. [CrossRef]
12. Parkinson, C.L.; Comiso, J.C.; Zwally, H.J.; Cavalieri, D.J.; Gloersen, P.; Campbell, W.J. *Arctic Sea Ice, 1973–1976: Satellite Passive-Microwave Observations*; Scientific and Technical Information Branch, National Aeronautics and Space Administration, 1987. Available online: https://ntrs.nasa.gov/citations/19870015437 (accessed on 6 December 2022).
13. Zwally, H.J. *Antarctic Sea Ice, 1973–1976: Satellite Passive-Microwave Observations*; Scientific and Technical Information Branch, National Aeronautics and Space, 1983; Volume 459. Available online: https://ntrs.nasa.gov/citations/19840002650 (accessed on 6 December 2022).
14. Chen, Y.; Zhao, X.; Pang, X.; Ji, Q. Daily sea ice concentration product based on brightness temperature data of FY-3D MWRI in the Arctic. *Big Earth Data* **2022**, *6*, 164–178. [CrossRef]
15. Chen, Y.; Zhao, X.; Lei, R.; Wu, S.; Liu, Y.; Fan, P.; Ji, Q.; Zhang, P.; Pang, X. A new Sea Ice Concentration Product in the Polar regions Derived from the FengYun-3 MWRI Sensors. *Earth Syst. Sci. Data Discuss* **2022**, 1–25. [CrossRef]
16. Zhao, X.; Chen, Y.; Kern, S.; Qu, M.; Ji, Q.; Fan, P.; Liu, Y. Sea Ice Concentration Derived From FY-3D MWRI and Its Accuracy Assessment. *IEEE Trans. Geosci. Remote Sens.* **2021**, *60*, 1–18. [CrossRef]
17. Shi, L.; Liu, S.; Shi, Y.; Ao, X.; Wang, Q. Sea Ice Concentration Products over Polar Regions with Chinese FY3C/MWRI Data. *Remote Sens.* **2021**, *13*, 2174. [CrossRef]
18. Witze, A. Ageing satellites put crucial sea-ice climate record at risk. *Nature* **2017**, *551*, 13–14. [CrossRef]
19. Cavalieri, D.J.; Gloersen, P.; Campbell, W.J. Determination of sea ice parameters with the NIMBUS 7 SMMR. *J. Geophys. Res. Atmos.* **1984**, *89*, 5355–5369. [CrossRef]
20. Comiso, J.C. *Enhanced Sea Ice Concentrations from Passive Microwave Data*; NASA Goddard Space Flight Center: Greenbelt, MD, USA, 2007.

21. Comiso, J. *SSM/I Sea Ice Concentrations Using the Bootstrap Algorithm*; National Aeronautics and Space Administration, Goddard Space Flight Center: Greenbelt, MD, USA, 1995; p. 1380. [CrossRef]

22. Comiso, J.C.; Sullivan, C.W. Satellite microwave and in situ observations of the Weddell Sea ice cover and its marginal ice zone. *J. Geophys. Res. Ocean.* **1986**, *91*, 9663–9681. [CrossRef]

23. Comiso, J.C. Characteristics of Arctic winter sea ice from satellite multispectral microwave observations. *J. Geophys. Res. Ocean.* **1986**, *91*, 975–994. [CrossRef]

24. Smith, D.M. Extraction of winter total sea-ice concentration in the Greenland and Barents Seas from SSM/I data. *Int. J. Remote Sens.* **1996**, *17*, 2625–2646. [CrossRef]

25. Lavergne, T.; Sørensen, A.; Kern, S.; Tonboe, R.; Notz, D.; Aaboe, S.; Bell, L.; Dybkjaer, G.; Eastwood, S.; Gabarro, C.; et al. Version 2 of the EUMETSAT OSI SAF and ESA CCI sea-ice concentration climate data records. *Cryosphere* **2019**, *13*, 49–78. [CrossRef]

26. Tonboe, R.; Eastwood, S.; Lavergne, T.; Sørensen, A.; Rathmann, N.; Dybkjaer, G.; Pedersen, L.; Høyer, J.; Kern, S. The EUMETSAT sea ice concentration climate data record. *Cryosphere* **2016**, *10*, 2275–2290. [CrossRef]

27. Brucker, L.; Cavalieri, D.J.; Markus, T.; Ivanoff, A. NASA Team 2 Sea Ice Concentration Algorithm Retrieval Uncertainty. *Geosci. Remote Sens.* **2014**, *52*, 7336–7352. [CrossRef]

28. Markus, T.; Cavalieri, D. An enhancement of the NASA Team sea ice algorithm. *Geosci. Remote Sens. IEEE Trans.* **2000**, *38*, 1387–1398. [CrossRef]

29. Spreen, G.; Kaleschke, L.; Heygster, G. Sea ice remote sensing using AMSR-E 89-GHz channels. *J. Geophys. Res. Ocean.* **2008**, *113*. [CrossRef]

30. Svendsen, E.; Matzler, C.; Grenfell, T.C. A model for retrieving total sea ice concentration from a spaceborne dual-polarized passive microwave instrument operating near 90 GHz. *Int. J. Remote Sens.* **1987**, *8*, 1479–1487. [CrossRef]

31. Kern, S.; Lavergne, T.; Notz, D.; Pedersen, L.T.; Tonboe, R.T.; Saldo, R.; Sørensen, A.M. Satellite passive microwave sea-ice concentration data set intercomparison: Closed ice and ship-based observations. *Cryosphere* **2019**, *13*, 3261–3307. [CrossRef]

32. Comiso, J.C.; Meier, W.N.; Gersten, R. Variability and trends in the Arctic Sea ice cover: Results from different techniques. *J. Geophys. Res. Ocean.* **2017**, *122*, 6883–6900. [CrossRef]

33. Ivanova, N.; Johannessen, O.M.; Pedersen, L.T.; Tonboe, R.T. Retrieval of Arctic Sea Ice Parameters by Satellite Passive Microwave Sensors: A Comparison of Eleven Sea Ice Concentration Algorithms. *IEEE Trans. Geosci. Remote Sens.* **2014**, *52*, 7233–7246. [CrossRef]

34. Pang, X.; Pu, J.; Zhao, X.; Ji, Q.; Qu, M.; Cheng, Z. Comparison between AMSR2 Sea Ice Concentration Products and Pseudo-Ship Observations of the Arctic and Antarctic Sea Ice Edge on Cloud-Free Days. *Remote Sens.* **2018**, *10*, 317.

35. Wiebe, H.; Heygster, G.; Markus, T. Comparison of the ASI Ice Concentration Algorithm With Landsat-7 ETM+ and SAR Imagery. *IEEE Trans. Geosci. Remote Sens.* **2009**, *47*, 3008–3015. [CrossRef]

36. Meier, W.N. Comparison of passive microwave ice concentration algorithm retrievals with AVHRR imagery in arctic peripheral seas. *IEEE Trans. Geosci. Remote Sens.* **2005**, *43*, 1324–1337. [CrossRef]

37. Agnew, T.; Howell, S. The use of operational ice charts for evaluating passive microwave ice concentration data. *Atmos. Ocean.* **2003**, *41*, 317–331. [CrossRef]

38. Agnew, T.A.; Howell, S. Comparison of digitized Canadian ice charts and passive microwave sea-ice concentrations. In Proceedings of the IEEE International Geoscience and Remote Sensing Symposium, Kuala Lumpur, Malaysia, 17–22 July 2002; pp. 231–233.

39. Zong, F.; Zhang, S.; Chen, P.; Yang, L.; Shao, Q.; Zhao, J.; Wei, L. Evaluation of Sea Ice Concentration Data Using Dual-Polarized Ratio Algorithm in Comparison With Other Satellite Passive Microwave Sea Ice Concentration Data Sets and Ship-Based Visual Observations. *Front. Environ. Sci.* **2022**, *10*, 278. [CrossRef]

40. Beitsch, A.; Kern, S.; Kaleschke, L. Comparison of SSM/I and AMSR-E Sea Ice Concentrations With ASPeCt Ship Observations Around Antarctica. *IEEE Trans. Geosci. Remote Sens.* **2015**, *53*, 1985–1996. [CrossRef]

41. Ozsoy-Cicek, B.; Xie, H.; Ackley, S.; Ye, K. Antarctic summer sea ice concentration and extent: Comparison of ODEN 2006 ship observations, satellite passive microwave and NIC sea ice charts. *Cryosphere* **2009**, *3*, 1–9. [CrossRef]

42. Knuth, M.A.; Ackley, S.F. Summer and early-fall sea-ice concentration in the Ross Sea: Comparison of in situ ASPeCt observations and satellite passive microwave estimates. *Ann. Glaciol.* **2006**, *44*, 303–309. [CrossRef]

43. Ivanova, N.; Pedersen, L.T.; Tonboe, R.T.; Kern, S.; Heygster, G.; Lavergne, T.; Sørensen, A.; Saldo, R.; Dybkjær, G.; Brucker, L.J.T.C. Inter-comparison and evaluation of sea ice algorithms: Towards further identification of challenges and optimal approach using passive microwave observations. *Cryosphere* **2015**, *9*, 1797–1817. [CrossRef]

44. Kern, S.; Lavergne, T.; Pedersen, L.; Tonboe, R.; Bell, L.; Meyer, M.; Zeigermann, L. Satellite passive microwave sea-ice concentration data set intercomparison using Landsat data. *Cryosphere* **2022**, *16*, 349–378. [CrossRef]

45. Cavalieri, D.; Parkinson, C.; Gloersen, P.; Zwally, H. *Sea Ice Concentrations from Nimbus-7 SMMR and DMSP SSM/ISSMI Passive Microwave Data, Version 1 [Data Set]*; NASA National Snow and Ice Data Center Distributed Active Archive Center: Boulder, CO, USA, 1996. [CrossRef]

46. Comiso, J. *Bootstrap Sea Ice Concentrations from Nimbus-7 SMMR and DMSP SSM/I-SSMIS, Version 3 [Data Set]*; NASA National Snow and Ice Data Center Distributed Active Archive Center: Boulder, CO, USA, 2017. [CrossRef]

47. Worby, A.; Comiso, J.C. Studies of the Antarctic sea ice edge and ice extent from satellite and ship observations. *Remote Sens. Environ.* **2004**, *92*, 98–111. [CrossRef]

48. Comiso, J.C.; Cavalieri, D.J.; Parkinson, C.L.; Gloersen, P. Passive microwave algorithms for sea ice concentration: A comparison of two techniques. *Remote Sens. Environ.* **1997**, *60*, 357–384. [CrossRef]
49. Matzler, C.; Ramseier, R.; Svendsen, E. Polarization effects in seaice signatures. *IEEE J. Ocean. Eng.* **1984**, *9*, 333–338. [CrossRef]
50. Cavalieri, D.J.; Parkinson, C.L.; Gloersen, P.; Zwally, H.J. Arctic and Antarctic Sea Ice Concentrations from Multichannel Passive-Microwave Satellite Data Sets: October 1978–September 1995 User's Guide. 1997. Available online: https://ntrs.nasa.gov/citations/19980076134 (accessed on 6 December 2022).
51. Andersen, S.; Tonboe, R.; Kaleschke, L.; Heygster, G.; Pedersen, L. Intercomparison of passive microwave sea ice concentration retrievals over the high-concentration Arctic sea ice. *J. Geophys. Res.* **2007**, *112*. [CrossRef]